

RESEARCH ARTICLE

SPECIAL ISSUE: CELL AND TISSUE POLARITY

Fat2 polarizes Lar and Sema5c to coordinate the motility of collectively migrating epithelial cells

Audrey Miller Williams¹ and Sally Horne-Badovinac^{1,2,*}

ABSTRACT

Migrating epithelial cells globally align their migration machinery to achieve tissue-level movement. Biochemical signaling across leading-trailing cell–cell interfaces can promote this alignment by partitioning migratory behaviors like protrusion and retraction to opposite sides of the interface. However, how signaling proteins become organized at interfaces to accomplish this is poorly understood. The follicular epithelial cells of *Drosophila melanogaster* have two signaling modules at their leading-trailing interfaces — one composed of the atypical cadherin Fat2 (also known as Kugelei) and the receptor tyrosine phosphatase Lar, and one composed of Semaphorin5c and its receptor Plexin A. Here, we show that these modules form one interface signaling system with Fat2 at its core. Trailing edge-enriched Fat2 concentrates both Lar and Semaphorin5c at leading edges of cells, but Lar and Semaphorin5c play little role in the localization of Fat2. Fat2 is also more stable at interfaces than Lar or Semaphorin5c. Once localized, Lar and Semaphorin5c act in parallel to promote collective migration. We propose that Fat2 serves as the organizer of this interface signaling system by coupling and polarizing the distributions of multiple effectors that work together to align the migration machinery of neighboring cells.

KEY WORDS: Collective cell migration, Planar cell polarity, Epithelium, *Drosophila*, Egg chamber

INTRODUCTION

Epithelial cells migrate collectively during animal development, wound healing, intestinal turnover and cancer metastasis (Friedl and Gilmour, 2009; Rørth, 2012; Theveneau and Mayor, 2013; Shaw and Martin, 2016; Krndjija et al., 2019). To do so, they must polarize within the epithelial plane at both the individual and tissue scales. At the individual scale, cells polarize along a leading-trailing axis. Protrusion and adhesion formation are biased to the leading edges of cells, and contractility and adhesion removal to their trailing edges, much as in cells migrating solo (Sherrard et al., 2021; Stock and Pauli, 2021; Soans et al., 2022). At the tissue scale, cells throughout the epithelium are polarized, such that their leading edges preferentially point in the direction of migration, and trailing edges in the opposite direction, a form of planar cell polarity. At the intersection of these scales are the cell–cell interfaces that link the trailing edge of one cell to the leading edge of the cell behind. These leading-trailing

interfaces can act as sites of biochemical or mechano-chemical signaling that polarize motility behaviors across the interface (Venhuizen and Zegers, 2017; Jain et al., 2020; Gupta and Yap, 2021; Roberto and Emery, 2022). However, we know little about how signaling proteins become organized along interfaces to accomplish this feat.

The rotational migration of the follicle cells in *Drosophila melanogaster* has proven to be a fruitful system for identifying signaling mechanisms that coordinate epithelial cell movements. Follicle cells are somatic cells of the egg chamber, the multicellular structure within the ovary that gives rise to an egg. They form a continuous monolayer epithelium around a central cluster of germ cells, and they are surrounded in turn by a basement membrane extracellular matrix that encapsulates the entire egg chamber. The apical surfaces of the follicle cells adhere to the germ cells, and their basal surfaces adhere to and crawl along the basement membrane (Haigo and Bilder, 2011; Cetera et al., 2014). Migration in this topologically closed configuration causes the entire egg chamber to rotate within the stationary basement membrane. This motion changes the structure of the basement membrane, ultimately helping give the egg its elongated shape (Gutzeit et al., 1991; Haigo and Bilder, 2011; Isabella and Horne-Badovinac, 2016; Crest et al., 2017). Follicle cell migration requires WAVE complex-dependent lamellipodia, which are polarized to the leading edge of each cell and planar-polarized across the epithelium (Gutzeit et al., 1991; Cetera et al., 2014) (Fig. 1A,B). Polarity emerges tissue-autonomously, without input from extrinsic directional cues. This simplifying feature allows us to more easily isolate the contribution of within-group coordination to collective migration. It likely also makes these cells particularly reliant on such coordination for movement.

Two biochemical signaling modules operate at leading-trailing interfaces, where they coordinate the migratory behaviors of neighboring follicle cells. The first module is composed of the atypical cadherin Fat2 (also known as Kugelei) and the receptor tyrosine phosphatase Leukocyte-antigen-related-like (Lar). Fat2 is enriched along the trailing edge of each cell, where it acts in trans to concentrate Lar and the WAVE complex across the cell–cell interface, at the leading edge of the cell behind (Viktorinová and Dahmann, 2013; Barlan et al., 2017; Williams et al., 2022) (Fig. 1C,D). Lar also contributes to WAVE complex localization, but not as strongly as Fat2, implying the existence of additional unidentified Fat2 effectors (Squarr et al., 2016; Barlan et al., 2017). Together, these proteins restrict cell protrusive activity to a single leading-edge domain and orient the protrusions from all the cells in a uniform direction across the tissue (Williams et al., 2022). The second module is composed of a transmembrane semaphorin (ligand) and plexin (receptor) pair, Semaphorin 5c (Sema5c) and Plexin A (PlexA), which are enriched at leading and trailing edges respectively (Stedden et al., 2019) (Fig. 1C,D). In other contexts, semaphorin–plexin signaling can lower integrin-based adhesion and/or inhibit protrusivity on the plexin-containing cell side (Hung and Terman, 2011;

¹Department of Molecular Genetics and Cell Biology, University of Chicago, Chicago, IL 60637, USA. ²Committee on Development, Regeneration, and Stem Cell Biology, University of Chicago, Chicago, IL 60637, USA.

*Author for correspondence (shorne@uchicago.edu)

 A.M.W., 0000-0001-6170-3365; S.H., 0000-0002-0473-7451

Handling Editor: David Bryant

Received 16 March 2023; Accepted 24 July 2023

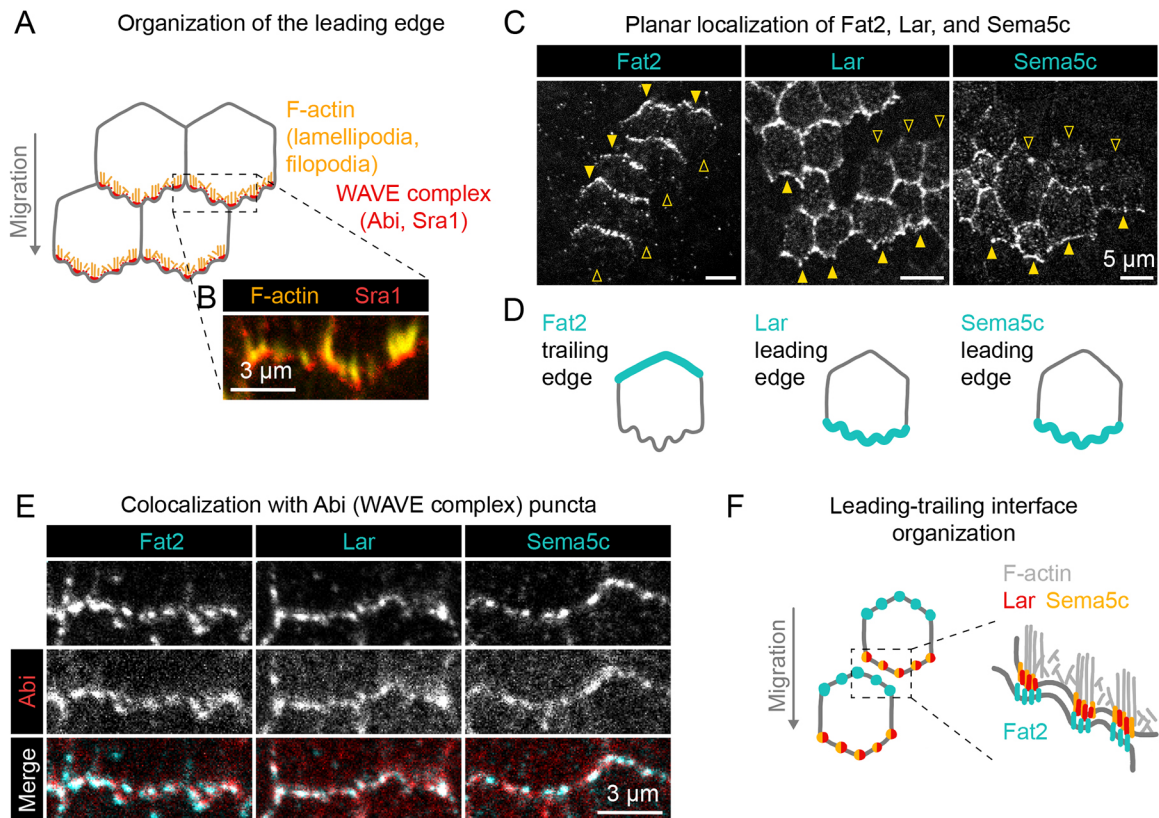


Fig. 1. Introduction to the organization of Fat2, Lar and Sema5c at the basal surface of the follicular epithelium. (A) Diagram of protrusion organization at the basal surface of four follicle cells. The WAVE complex (including subunits Abi and Sra1, labeled in this study) is enriched at the tips of filopodia and lamellipodia along the leading edge of each cell. (B) Image of the leading edge of one cell with Sra1 (Sra1-GFP) and F-actin (phalloidin) labeled. Filopodia are the most prominent F-actin structures. (C) Images of the basal surfaces of epithelia with mosaic expression of Fat2-3×GFP, Lar-3×GFP or Sema5c-3×GFP, showing the cell side to which each is polarized. Arrowheads point to leading-trailing interfaces at the boundary between 3×GFP-labeled and unlabeled cells. Arrowheads are filled yellow where the labeled protein is enriched and hollow elsewhere. (D) Diagrams of Fat2, Lar, and Sema5c localization at the basal surface, as shown in C. Fat2 is polarized to the trailing edge; Lar and Sema5c to the leading edge. (E) Images of leading-trailing interfaces labeled with Abi-mCherry and Fat2-3×GFP, Lar-3×GFP or Sema5c-3×GFP. (F) Diagram showing the organization of a leading-trailing interface. Fat2, Lar and Sema5c molecules reside together in puncta that span leading and trailing edges, with Fat2 enriched at the trailing edge and Lar and Sema5c at the leading edge.

Alto and Terman, 2017; Verhagen and Pasterkamp, 2020). Similarly, overexpression of Sema5c in one follicle cell reduces the protrusivity of its neighbors in a PlexA-dependent manner (Stedden et al., 2019). This led to the model that Sema5c signals through PlexA to maintain a non-protrusive state at the trailing edges of cells.

Despite their distinct depletion and overexpression phenotypes, several lines of evidence suggest that the Fat2-Lar and Sema5c-PlexA modules function within one interface-polarizing signaling system. A series of pairwise comparisons show that Fat2, Lar and Sema5c all colocalize with the WAVE complex in interface-spanning puncta that sit at the tips of filopodia within a broader lamellipodium (Squarr et al., 2016; Barlan et al., 2017; Stedden et al., 2019; Williams et al., 2022) (Fig. 1E,F). For reasons that are not yet clear, PlexA only rarely colocalizes with the other proteins (Stedden et al., 2019). Loss of Lar also reduces the enrichment of Sema5c at leading edges (Stedden et al., 2019), implying functional interaction between the two modules in addition to their shared spatial organization. In this study, we investigated the hierarchy of interactions between Fat2, Lar, and Sema5c by which they form interface-spanning puncta, and asked how the three proteins work together to promote collective migration.

We find that Fat2 forms the core of both the Lar and Sema5c-containing signaling modules, concentrating Sema5c at leading

edges in trans as it was previously shown to do for Lar. Conversely, Lar and Sema5c play little or no role in the localization of Fat2. Using fluorescence recovery after photobleaching (FRAP) and acute inhibition experiments, we show that Fat2 resides more stably at trailing edges than do Lar or Sema5c at leading edges, and that Fat2 is likely continuously required to maintain the enrichment of Lar and Sema5c at leading edges in the face of their ongoing turnover. We further find that Lar and Sema5c act in parallel to promote collective migration. From these data, we propose that Fat2 acts as a central organizer of the follicle cell interface-polarizing signaling system, serving to couple and polarize the distributions of multiple effectors that together align the motility machinery of neighboring cells.

RESULTS

Fat2 concentrates Sema5c at leading edges as it was previously shown to do for Lar

Fat2, Lar and Sema5c all colocalize in interface-spanning puncta, with Fat2 at trailing edges and Lar and Sema5c at leading edges (Viktorinová and Dahmann, 2013; Barlan et al., 2017; Stedden et al., 2019). Fat2 acts in trans to concentrate Lar at leading edges (Barlan et al., 2017), a result we confirmed in this study using a new endogenous 3×GFP tag on Lar (Fig. S1). To ask whether Fat2 has

the same effect on Sema5c, we generated epithelia with mosaic expression of *fat2*-RNAi, which allowed us to analyze Sema5c-3×GFP levels along leading-trailing interfaces at the basal surfaces of epithelia in which tissue-wide planar polarity was preserved. Sema5c levels were reduced wherever a *fat2*-RNAi cell was present ahead of the interface, regardless of the genotype of the cell behind the interface (Fig. 2A,B), again indicating a local trans interaction. This effect was sufficiently strong to eliminate all enrichment of

Sema5c at leading-trailing interfaces relative to side interfaces (Fig. S2A). Given that Lar also contributes to the enrichment of Sema5c at leading edges (Stedden et al., 2019), we asked whether Fat2 localizes Sema5c indirectly through Lar. We confirmed that Sema5c levels were indeed reduced at leading-trailing interfaces between control cells and cells with a null *lar* allele (*lar*^{13.2}, Fig. 2C,D). However, this reduction was not as great as at interfaces between *fat2*-RNAi cells (Fig. 2E). In addition, if Fat2

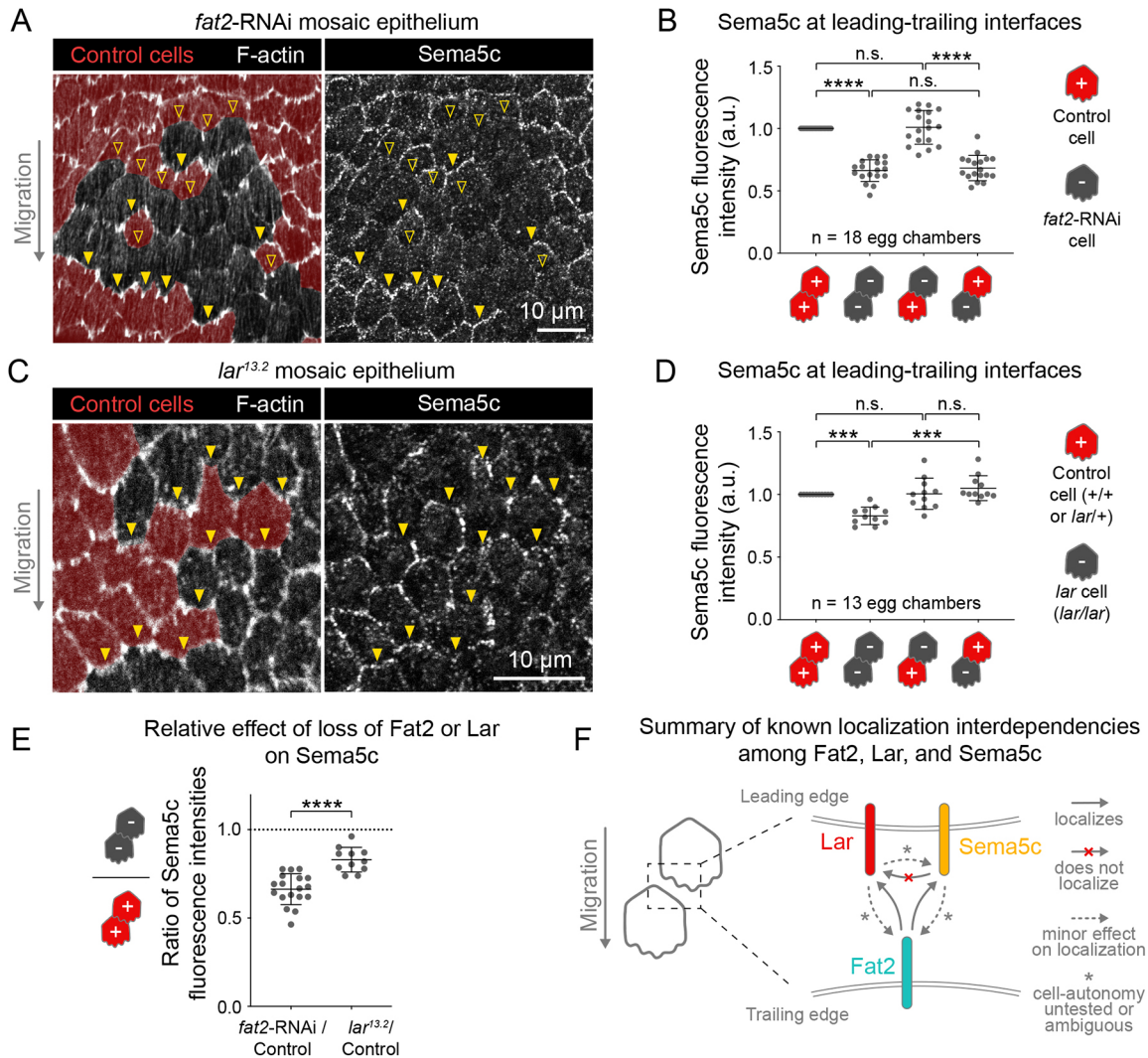


Fig. 2. Fat2 concentrates Sema5c in trans at the leading edge. (A) Images of a *fat2*-RNAi mosaic epithelium expressing Sema5c-3×GFP, with F-actin stained using phalloidin. Control cells are pseudo-colored based on genetically encoded markers. Filled yellow arrowheads indicate leading edges of *fat2*-RNAi-expressing cells behind control cells, which have normal Sema5c-3×GFP enrichment. Hollow arrowheads indicate the leading edges of control cells behind *fat2*-RNAi-expressing cells, which have reduced Sema5c-3×GFP enrichment. (B) Plot of Sema5c-3×GFP fluorescence intensity at leading-trailing interfaces between different combinations of control and *fat2*-RNAi-expressing cells. Bars indicate mean±s.d. Sema5c-3×GFP enrichment is reduced at the leading edge of cells of any genotype behind *fat2*-RNAi cells. n.s., not significant, $P=0.99, 0.79$ (left to right); **** $P<0.0001$ [repeated measures one-way ANOVA ($F(2.42, 41.07)=96.23, P<0.0001$ with post-hoc Tukey's test)]. (C) Images of a *lar*^{13.2} mosaic epithelium expressing Sema5c-3×GFP, with F-actin stained using phalloidin. Control cells are pseudo-colored based on genetically encoded markers. Arrowheads indicate leading-trailing interfaces at boundaries between control and *lar*^{13.2} cells in either order, both of which are enriched for Sema5c-3×GFP. (D) Plot of Sema5c-3×GFP fluorescence intensity at leading-trailing interfaces between different combinations of control and *lar*^{13.2} cells. Bars indicate mean±s.d. Sema5c-3×GFP enrichment is reduced at leading-trailing interfaces between two *lar*^{13.2} cells, but not at interfaces with a control cell either ahead or behind, which is inconsistent with Lar simply recruiting Sema5c locally to their shared leading edge. n.s., not significant, $P>0.99, 0.77$ (left to right), *** $P=0.003$, **** $P<0.0001$ [repeated measures one-way ANOVA ($F(2.24, 22.41)=19.93, P<0.0001$ with post-hoc Tukey's test)]. (E) Plot comparing the effects of loss of Fat2 and Lar on Sema5c-3×GFP enrichment at leading-trailing interfaces. Data replotted from B and D. Both *fat2*-RNAi and *lar*^{13.2} reduce Sema5c-3×GFP enrichment (fluorescence intensity ratios below dotted line at $y=1$), but *fat2*-RNAi causes a greater reduction. **** $P<0.0001$ (unpaired two-tailed t -test). (F) Diagram showing dependencies among Fat2, Lar and Sema5c for localization to the leading-trailing interface, summarizing findings from this and previous studies (Barlan et al., 2017; Stedden et al., 2019) (see also Fig. 5, Fig. S1D,E). Fat2 concentrates Lar and Sema5c at the leading edge in trans, and Lar and Sema5c play minor, perhaps non-interface-local roles in the distribution of the three proteins. a.u., arbitrary units.

localized Sema5c through Lar, because Fat2 concentrates Lar and Sema5c in trans to leading edges, we would expect Lar to concentrate Sema5c in cis. However, Sema5c levels were only reduced at leading-trailing interfaces between two *lar*^{13.2} cells, indicating that the localization relationship between Lar and Sema5c is more complex. We conclude that Fat2 acts in trans to concentrate Sema5c at leading edges at least partly independently of Lar (Fig. 2F). We also found that Fat2-induced localization of Sema5c is not mediated by the WAVE complex or protrusions (Fig. S2B,C).

We next asked whether Fat2 is continuously required for the enrichment of Lar and Sema5c at leading edges, or whether it becomes dispensable after interface polarity is established. Because Ca²⁺ ions are integral to the structure of cadherin extracellular domains (Nagar et al., 1996; Kim et al., 2011; Tsukasaki et al., 2014), Ca²⁺ removal should disrupt any Fat2 function that depends directly or indirectly on its extracellular domain. Treating egg chambers with the cell-impermeable Ca²⁺ chelator ethylene glycol-O,O'-bis(2-aminoethyl)-N,N,N',N'-tetraacetic acid (EGTA, 20 mM) for 5 min reduced the levels of protrusion-associated F-actin (Fig. 3A), consistent with loss of Fat2 function (Squarr et al., 2016; Barlan et al., 2017) (compare to Fig. 2A, Fig. S1D). It did not, however, cause other obvious changes to cell morphology, and protrusions returned within 1 h after EGTA washout (Fig. 3A), suggesting that this method rapidly and reversibly inhibits Fat2 without generally disrupting tissue architecture. However, it is likely that other cadherins and extracellular Ca²⁺-dependent molecules are also being affected by EGTA treatment, which could contribute to observed phenotypes. Notably, the 5-min EGTA treatment substantially reduced Lar and Sema5c levels along leading-trailing interfaces (Lar fluorescence intensity by 50%, Sema5c by 25%; Fig. 3B,C). Fat2 levels were nearly unchanged after 5 min, but its distribution became even more punctate, and by 30 min of EGTA treatment its levels had substantially decreased (Fig. 3B–D). Thus, Fat2 appears to be continuously required to maintain the enrichment of Lar and Sema5c at leading edges, although more specific methods for acute inhibition of Fat2 will be required to confirm this conclusion.

To probe the limits of the capacity of Fat2 to position the leading-edge proteins, we used GrabFP-A^{Int} to create an ectopic Fat2 population (Harmansa et al., 2017) (Fig. 4A), and asked whether this could relocalize Lar. At present, we lack a functional Sema5c antibody, and so could not check for its relocalization. Fat2 and Lar normally colocalize in puncta at the basal surface and along tricellular junctions that span the apical-basal axis (Viktorinová et al., 2009; Bateman et al., 2001). Expression of GrabFP-A^{Int} caused Fat2–3×GFP to accumulate all around adherens junctions as well, and increased Fat2–3×GFP levels overall (Fig. 4B–F). The ectopic Fat2 had no effect on the distribution of Lar, which remained restricted to tricellular junctions in the adherens junction plane despite Fat2 being all around the cell perimeter (Fig. 4D–F). These data show that although Fat2 is absolutely required for enrichment of Lar at leading edges, it is limited in its ability to recruit Lar, implying that other proteins or cell features also help shape the distribution of Lar.

Lar and Sema5c play only a minor role in the localization of Fat2

Given the importance of Fat2 for localizing Lar and Sema5c, we asked whether they play a reciprocal role in localizing Fat2. We previously used a *lar* mutant condition to show that Lar plays little or no role in the localization of Fat2. Here, we confirmed this finding using *lar*-RNAi, and then examined the effect of loss of Sema5c or

both proteins together on the localization of Fat2. To this end, we measured the average level of Fat2–3×GFP along all cell–cell interfaces at the basal surface of epithelia lacking Lar (*lar*-RNAi), Sema5c (*Sema5c*^{K175}) or both proteins together (*lar*-RNAi, *Sema5c*^{K175}) and compared these values to control epithelia. Full basal cell perimeters were used instead of leading-trailing interfaces because Fat2 loses its planar polarization when migration is disrupted (Barlan et al., 2017), as occurs in some of these backgrounds (see Fig. 7). Fat2 levels were normal in epithelia lacking Lar and mildly reduced in epithelia lacking Sema5c (Fig. 5A–C). Importantly, Fat2 levels were not further reduced in epithelia lacking both proteins compared to those lacking Sema5c alone (Fig. 5A,B). So, whereas Fat2 plays a major role in localizing Lar and Sema5c, Lar and Sema5c play at most a minor role in localizing Fat2 (Fig. 2H).

Fat2 is more stable at leading-trailing interfaces than Lar or Sema5c

We next investigated the dynamics of Fat2, Lar and Sema5c turnover along leading-trailing interfaces, predicting that as a more central organizer, Fat2 would be more stable than the other proteins. To test this, we used FRAP to measure the turnover rate of each protein along leading-trailing interfaces at the basal surfaces of follicle cells. Within 6 min after photobleaching, Fat2–3×GFP fluorescence had only recovered to 29±10% of its initial levels, whereas Lar–3×GFP and Sema5c–3×GFP fluorescence had recovered to 70±21% and 90±26%, respectively (mean±s.d.; Fig. 6A,B,D; Movie 1). During a longer recovery period of 28 min, Fat2–3×GFP fluorescence reached 59±25% of initial levels, still lower than the maximum recovery seen for Lar and Sema5c (Fig. 6C,E; Movie 2). These data show that Fat2 molecules reside at leading-trailing interfaces for tens of minutes, and Lar and Sema5c only minutes, consistent with the more central role for Fat2 in interface organization.

We then asked whether Fat2 stabilizes Lar and Sema5c at interfaces by performing the same FRAP experiment in epithelia lacking Fat2, predicting that the turnover of Lar and Sema5c would increase in its absence (Fig. S3A–F). We found that in *fat2*^{N103-2} epithelia, the average time to half recovery of both Lar–3×GFP and Sema5c–3×GFP decreased (Fig. S3C,F). However, this decrease was not statistically significant for Lar–3×GFP, and in the case of Sema5c–3×GFP it was accompanied by a decrease in total recovery as well as an increase in the rate of recovery. Sema5c–3×GFP levels are lower than Lar–3×GFP under normal circumstances (Fig. S3G,H), and Lar–3×GFP and Sema5c–3×GFP levels at interfaces are reduced in the absence of Fat2 (see Fig. 2, Fig. S1), which might have limited our ability to resolve changes in their dynamics. Further work is needed to determine whether Fat2 stabilizes Lar and Sema5c at leading edges or concentrates them there through a different mechanism.

Lar and Sema5c promote collective migration in parallel downstream of Fat2

Fat2, Lar and Sema5c are all required for normal collective migration, but whereas loss of Fat2 prevents migration entirely, loss of Lar only slows migration, and loss of Sema5c both slows it and delays its onset (Viktorinová and Dahmann, 2013; Barlan et al., 2017; Stedden et al., 2019) (Fig. 7A,B). These milder migration phenotypes suggest that Lar and Sema5c might act in parallel downstream of Fat2 to regulate cell motility. If true, analysis of the cell-scale phenotypes caused by loss of Lar or Sema5c could help us understand the two ‘arms’ of the interface signaling system that Fat2 assembles. Fat2 promotes epithelial migration both by increasing

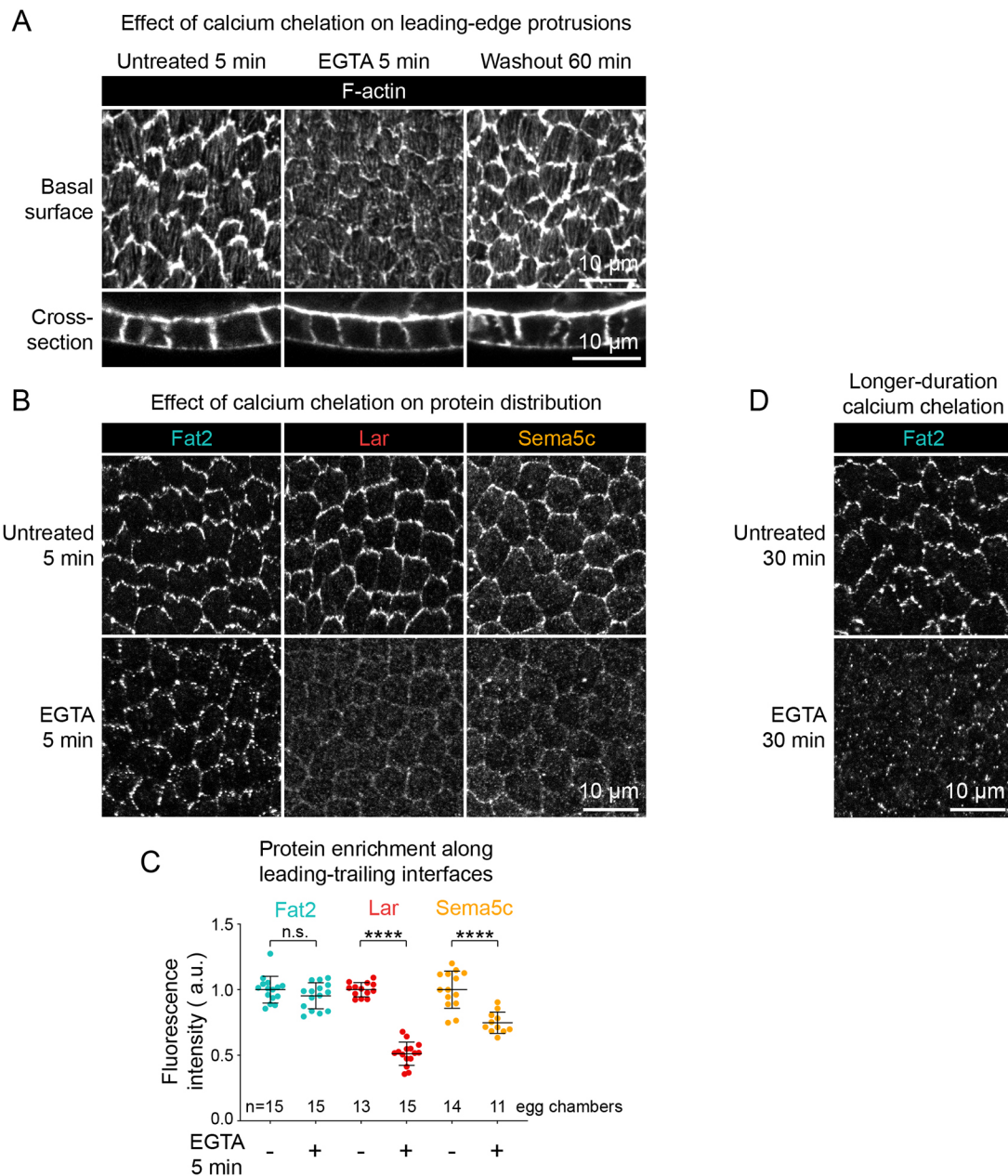


Fig. 3. Ca^{2+} chelation causes rapid loss of Lar and Sema5c from the leading edge. (A) Images of the basal surfaces of the follicle cells with F-actin stained by phalloidin after being left untreated for 5 min, treated with 20 mM EGTA (an extracellular Ca^{2+} chelator) for 5 min followed by washout and 60 min of recovery. F-actin-rich protrusions are reduced by EGTA treatment, but return following washout. Cross-section images show no apparent changes to follicle cell shape or epithelial integrity caused by EGTA treatment or treatment and washout. (B) Images of Fat2-, Lar- or Sema5c-3×GFP at the basal surfaces of epithelia left untreated or treated with 20 mM EGTA for 5 minutes, representative of data quantified in C. (C) Plot of the mean fluorescence intensity of Fat2-3×GFP, Lar-3×GFP, and Sema5c-3×GFP along leading-trailing interfaces at the basal surface, with or without 5 min of EGTA treatment. EGTA treatment causes a reduction in Lar- and Sema5c-3×GFP levels, but no significant change in Fat2-3×GFP levels. Bars indicate mean±s.d. n.s., not significant, $P=0.21$; **** $P<0.0001$ (unpaired two-tailed t -tests). (D) Images of Fat2-3×GFP at the basal surface of epithelia left untreated or treated with 20 mM EGTA for 30 minutes. Unlike in B and C, this longer treatment results in nearly complete clearance of Fat2-3×GFP from the basal surface. Images in A and D are representative of two experimental repeats. a.u., arbitrary units.

cell protrusivity and by polarizing protrusions of cells in the direction of tissue movement (Squarr et al., 2016; Barlan et al., 2017; Williams et al., 2022), so we asked whether Lar or Sema5c play similar roles in protrusion formation and polarity. These roles have previously been studied using F-actin labeling (Squarr et al., 2016; Barlan et al., 2017; Stedden et al., 2019), but we recently found that this approach misses much of the protrusive activity in *fat2*^{N103-2} epithelia (Williams et al., 2022). We therefore used live

imaging and membrane labeling to re-examine the protrusion phenotypes caused by loss of Lar or Sema5c alone, and to build on this by determining the effect of losing both proteins together. We performed automated segmentation of protrusions to measure the average cell protrusivity of epithelia and the polarity of those protrusions, as first described in Williams et al. (2022).

First, we examined the role of Lar in protrusion formation and polarity. F-actin staining had suggested that cells lacking Lar are less

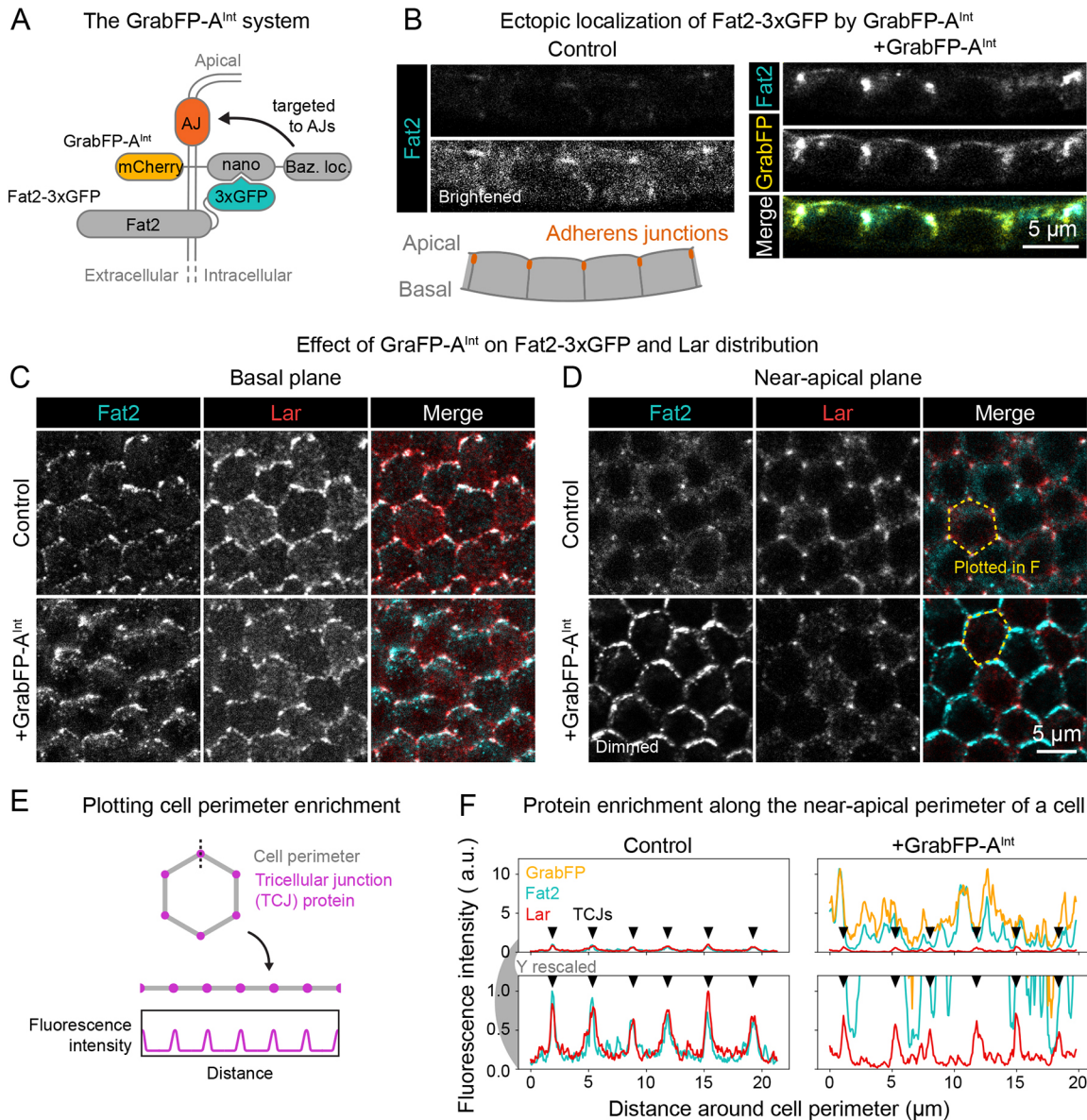


Fig. 4. Fat2 is not sufficient to relocate Lar away from the basal surface or tricellular junctions. (A) Diagram showing how the GrabFP-A^{Int} protein is used to recruit Fat2–3×GFP to adherens junctions (AJs). GrabFP-A^{Int} binds intracellularly GFP-tagged proteins with a GFP nanobody (nano), and is targeted to AJs, along with any bound proteins, by a domain of Bazooka (Baz. loc.). (B) Images of Fat2–3×GFP-expressing follicle cells in cross-section with or without expression of GrabFP-A^{Int}. Top row, Fat2 images have matched display settings for comparison of protein levels; Fat2 is displayed more brightly in the bottom-left image. The diagram shows the imaging plane, with the AJs to which GrabFP-A^{Int} is targeted indicated. Fat2–3×GFP is present in control cells, but its enrichment at adherens junctions and overall levels are strongly increased in the presence of GrabFP-A^{Int}. (C,D) Images of Fat2–3×GFP-expressing epithelia with or without co-expression of GrabFP-A^{Int}, stained with an anti-Lar antibody. Images in C show the basal planes of a group of cells; images in D show a near-apical plane through their adherens junctions. Fat2–3×GFP is displayed more dimly in the +GrabFP-A^{Int} image in D relative to other images to allow the Fat2–3×GFP distribution to be clear in each. (E) Diagram illustrating the ‘unrolling’ process by which the perimeters of cells such as those outlined in D are linearized for plotting in F. (F) Plots of the fluorescence intensity distribution of Fat2–3×GFP, anti-Lar and GrabFP-A^{Int} (if present) along the cell perimeters outlined in D. The upper row shows the full range of intensities, and the lower row shows an expanded view of the lower intensities. Triangles correspond to tricellular junctions (TCJs), to which Fat2 and Lar are normally largely restricted in this plane. GrabFP-A^{Int} expression causes a large increase in Fat2–3×GFP levels and their expansion around the entire cell perimeter, but Lar remains restricted to tricellular junctions. Images are representative of two experimental repeats. a.u., arbitrary units.

protrusive than normal (Squarr et al., 2016; Barlan et al., 2017). However, using membrane labeling, we detected no reduction in protrusivity in *lar*^{13.2/bola1} epithelia (Fig. 7C,D; Movie 3). This suggests that Lar increases F-actin enrichment within protrusions, but is not required for protrusion formation per se. Loss of Lar did, however, disrupt protrusion polarity. Whereas control epithelia had most protrusions pointed in the direction of migration, slowly

migrating *lar*^{13.2/bola1} epithelia had a sizeable minority pointed rearwards, and their protrusions were less aligned with migration overall (Fig. 7C,E; Fig. S4, Movie 3). We did not observe an increase in rearwards protrusions in slowly-migrating epithelia of other genotypes (see below; compare protrusion alignment of migratory *lar*^{13.2/bola1} and migratory *Sema5c*^{K175} epithelia in Fig. 7E), so it is unlikely that the increase in rearwards protrusions is an indirect effect

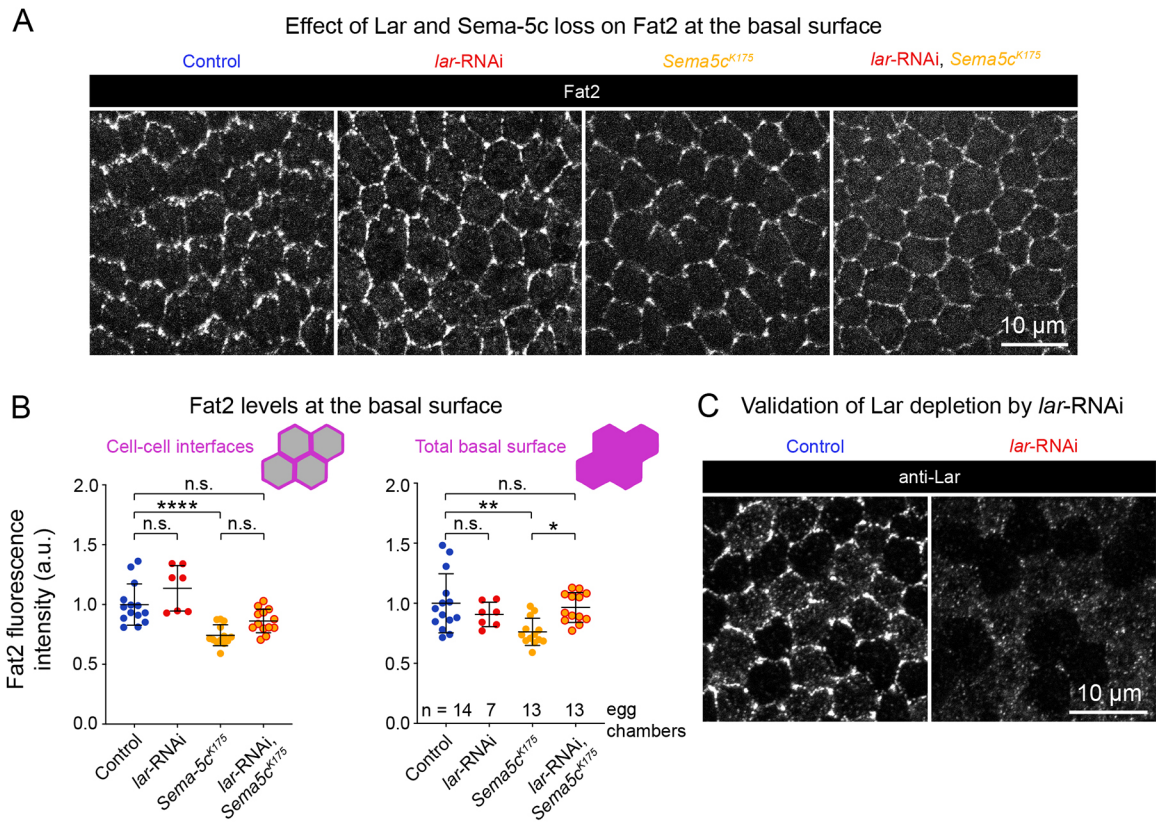


Fig. 5. The enrichment of Fat2 at interfaces shows only a mild dependence on Lar and Sema5c. (A) Images of Fat2–3×GFP at the basal surface in control epithelia, *lar*-RNAi-expressing or *Sema5c*^{K175} epithelia, and in a combined *Sema5c*^{K175} *lar*-RNAi-expressing epithelium. (B) Plots of Fat2–3×GFP levels at cell–cell interfaces (left) or the entire basal surface (right) of epithelia exemplified in A. Fat2–3×GFP levels are slightly reduced at interfaces and across the basal surface in *Sema5c*^{K175} epithelia. Lar depletion causes no additional reduction in Fat2–3×GFP levels at these locations. Bars indicate mean \pm s.d. Cell–cell interfaces: **** $P < 0.0001$, n.s., not significant, $P = 0.16$, 0.059 , 0.14 (left to right) [one-way ANOVA ($F(3,43) = 15.18$, $P < 0.0001$ with post-hoc Tukey's test)]. Total basal surface: ** $P = 0.0030$, * $P = 0.016$, n.s., not significant, $P = 0.63$, 0.95 (left to right) [one-way ANOVA ($F(3,43) = 5.31$, $P = 0.0033$ with post-hoc Tukey's test)]. (C) Images of Lar antibody staining at the basal surface, demonstrating the strength of Lar depletion by *lar*-RNAi. Images in C are representative of two experimental repeats. a.u., arbitrary units.

of the slow migration of the cells, but rather a local (cell or interface-scale) effect of loss of Lar. These data show that Lar helps polarize protrusions across the tissue and suggest that the role of Fat2 in this process is due in part to its ability to localize Lar.

We then performed the same analysis for Sema5c. *Sema5c*^{K175} epithelia initiate migration later in development than normal, and their migration is slow and difficult to preserve *ex vivo* (Stedden et al., 2019). Consistent with this, about half of the *Sema5c*^{K175} epithelia were migrating detectably, albeit slowly, and several others had a degree of protrusion polarity that likely indicated they had been migrating prior to dissection (Fig. 7A,B; Fig. S4B). In agreement with previous findings based on F-actin staining (Stedden et al., 2019), we did not observe a difference in the membrane protrusivity of *Sema5c*^{K175} epithelia. In the detectably migrating subset of epithelia, protrusion polarity also appeared normal (Fig. 7C–E; Fig. S4, Movie 3). The slow migration speeds of these epithelia therefore do not seem to be caused by protrusion defects, although it is possible that Sema5c regulates protrusions in ways we did not detect. Alternatively, Sema5c might primarily regulate other aspects of cell motility such as contractility or adhesion.

Finally, we asked whether Lar and Sema5c work in parallel to promote collective migration by expressing *lar*-RNAi in follicle cells of *Sema5c*^{K175} egg chambers. These epithelia failed to migrate and had unpolarized protrusions in all cases, and a significant speed reduction compared to epithelia lacking Lar or one of the two

conditions lacking Sema5c (Fig. 7A,B), which was indistinguishable from *fat2*^{N103-2} epithelia (Fig. 7A–C,E; Fig. S4; Movie 3). We conclude that Lar and Sema5c act in parallel to regulate cell motility, likely through distinct mechanisms. These data further suggest that Fat2-mediated polarization of both Lar and Sema5c to leading edges is a major means by which it regulates the collective migration of follicle cells.

DISCUSSION

The follicle cells use biochemical signaling across their leading-trailing interfaces to polarize their migration machinery at interface, cell and tissue scales. Here, we have shown that Fat2 is a central organizer of this signaling system. Fat2 acts at the trailing edge of each cell to concentrate both Lar and Sema5c at the leading edge of the cell behind. By contrast, Lar and Sema5c play at most minor roles in the localization of Fat2. In this way, Fat2 coordinates the activities of two effector proteins with distinct functions, allowing them to work synergistically to promote highly persistent collective migration.

One defining feature of this Fat2-based signaling system is that most of the component proteins colocalize in interface-spanning puncta. Cadherins often self-organize into clusters (Truong Quang et al., 2013; Wu et al., 2015; Brasch et al., 2019; Stahley et al., 2021), making it likely that this punctate organization stems from Fat2. However, whether Fat2 concentrates Lar and Sema5c in the

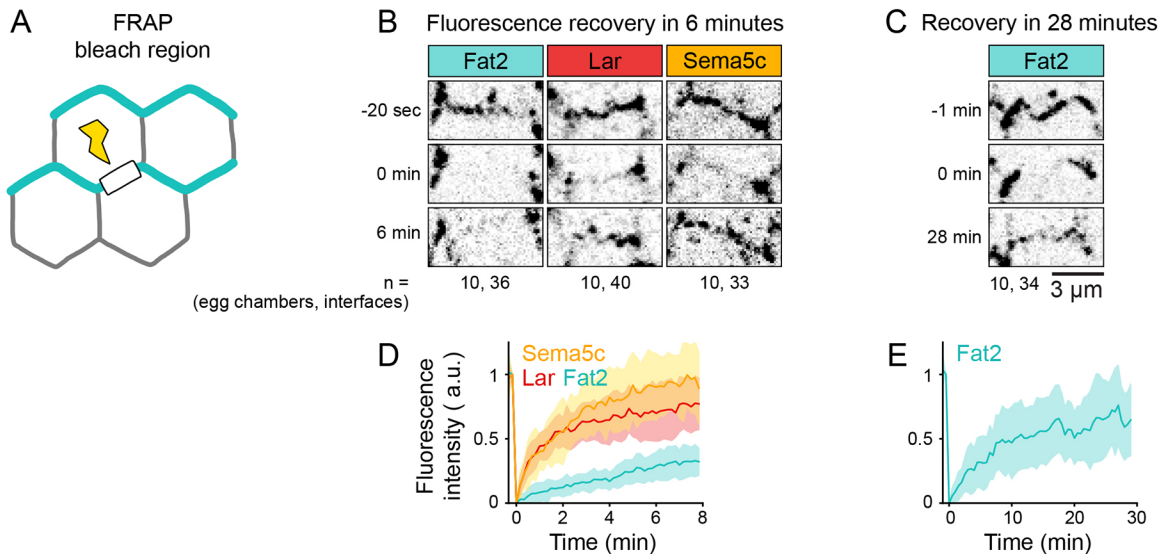


Fig. 6. Fat2 is relatively stable at the trailing edge; Lar and Sema5c exchange more rapidly from the leading edge. (A) Diagram of the photobleached regions: leading-trailing interfaces at the basal surface excluding the two bounding tricellular junctions. (B) Images of Fat2-3×GFP, Lar-3×GFP and Sema5c-3×GFP at individual leading-trailing interfaces shortly before, immediately after, and 6 min after photobleaching. (C) Images of Fat2-3×GFP at a leading-trailing interface shortly before, immediately after, and 28 minutes after photobleaching. (D) Plot comparing recovery of Fat2-3×GFP, Lar-3×GFP and Sema5c-3×GFP fluorescence intensity to leading-trailing interfaces over 8 min following photobleaching, for results as exemplified in B. Solid lines and filled regions show mean±s.d. Fat2 recovers more slowly than Lar or Sema5c. (E) Plot showing recovery of Fat2-3×GFP fluorescence intensity to leading-trailing interfaces over 28 min following photobleaching, for results as exemplified in C. In that time, its fluorescence had still only recovered to 65% of its initial level, less than Lar-3×GFP or Sema5c-3×GFP did within 8 min. a.u., arbitrary units.

puncta through direct binding or through intermediary proteins is unknown. An ectopic Fat2 pool did not cause redistribution of Lar, suggesting that additional inputs also contribute to the localization of Lar. We also do not know how the receptor for Sema5c, PlexA, fits into this model. Like Fat2, PlexA is enriched at the trailing edges of cells and helps to localize Sema5c, and yet antibody staining indicates that PlexA only partially colocalizes with the Fat2-based puncta (Stedden et al., 2019). The biggest open question is how Fat2 becomes localized to the trailing edge, as this appears to be the key event that polarizes the entire signaling system. Mechanical feedback from collective migration itself is required for the polarization of Fat2 to trailing edges (Barlan et al., 2017), but the nature of this feedback, and whether Fat2 has a trans binding partner that further stabilizes its localization, will be important areas for future investigation.

This study includes the first measurements of the dynamics of planar signaling proteins in follicle cells, which is an important step towards understanding their polarization mechanism. Using FRAP, we found that Fat2 is a more stable resident of the leading-trailing interface-spanning puncta than are Lar or Sema5c, consistent with its more central role in maintaining these structures. Based on these FRAP data, as well as the rapid redistribution of Lar and Sema5c upon extracellular Ca^{2+} chelation, we hypothesize that Fat2 maintains the leading edge enrichment of Lar and Sema5c by slowing their turnover within the puncta, thereby concentrating them at the leading edge. However, the continuous requirement of Fat2 for the maintenance of polarization of Lar and Sema5c awaits confirmation with a more specific method of acute Fat2 inhibition, as extracellular Ca^{2+} chelation is a blunt tool, and it is possible that Fat2-independent effects, such as the disruption of another cadherin, contributed to the rapid localization changes of Lar and Sema5c. Further comparison of the dynamics of Lar and Sema5c with and without Fat2 will also be needed to determine whether Fat2 concentrates them through local stabilization (for example through

direct or indirect binding) or by a different mechanism, such as increasing their rate of arrival at leading edges.

This work also sheds light on how Lar and Sema5c work together to promote collective migration. We have previously shown that loss of either protein alone impairs migration but does not stop it (Barlan et al., 2017; Stedden et al., 2019). By contrast, we now find that removing both proteins together fully blocks migration in a way that is indistinguishable from loss of Fat2. These data suggest that once Fat2 concentrates Lar and Sema5c to the leading edges of cells, they then act in parallel to promote collective migration, likely by polarizing distinct aspects of the migration machinery.

What aspects of the migration machinery do Lar and Sema5c each control? In the case of Lar, it seems to be part of the bridge between Fat2 and WAVE complex-dependent protrusions — both Fat2 and Lar increase protrusive F-actin enrichment at leading edges (Fat2 in trans and Lar in cis) (Squarr et al., 2016; Barlan et al., 2017), and both also help polarize protrusions in the direction of migration (Williams et al. (2022) and this study). In addition, Lar acts in trans to promote retraction of the trailing edge of the cell ahead (Barlan et al., 2017), but the mechanistic basis for this trans function and the degree to which it is separable from the cis function of Lar, remain undetermined. In the case of Sema5c, cell-scale loss-of-function phenotypes have proven more elusive, but enrichment of PlexA at trailing edges and the ability of overexpressed Sema5c to suppress protrusion in trans both point to the trailing edge as the likely site of regulation (Stedden et al., 2019).

By positioning both Lar and Sema5c, Fat2 integrates two features of interface signaling systems known to operate in other collectively migrating cell types but not yet seen together. The first feature is the use of a trailing edge-associated mechanical cue to orient protrusions in the cell behind (Das et al., 2015; Hayer et al., 2016). Mechanical localization of Fat2 to trailing edges polarizes protrusions in the following cell, in part by localizing Lar (Barlan et al., 2017). The second feature is the use of contact inhibition of locomotion

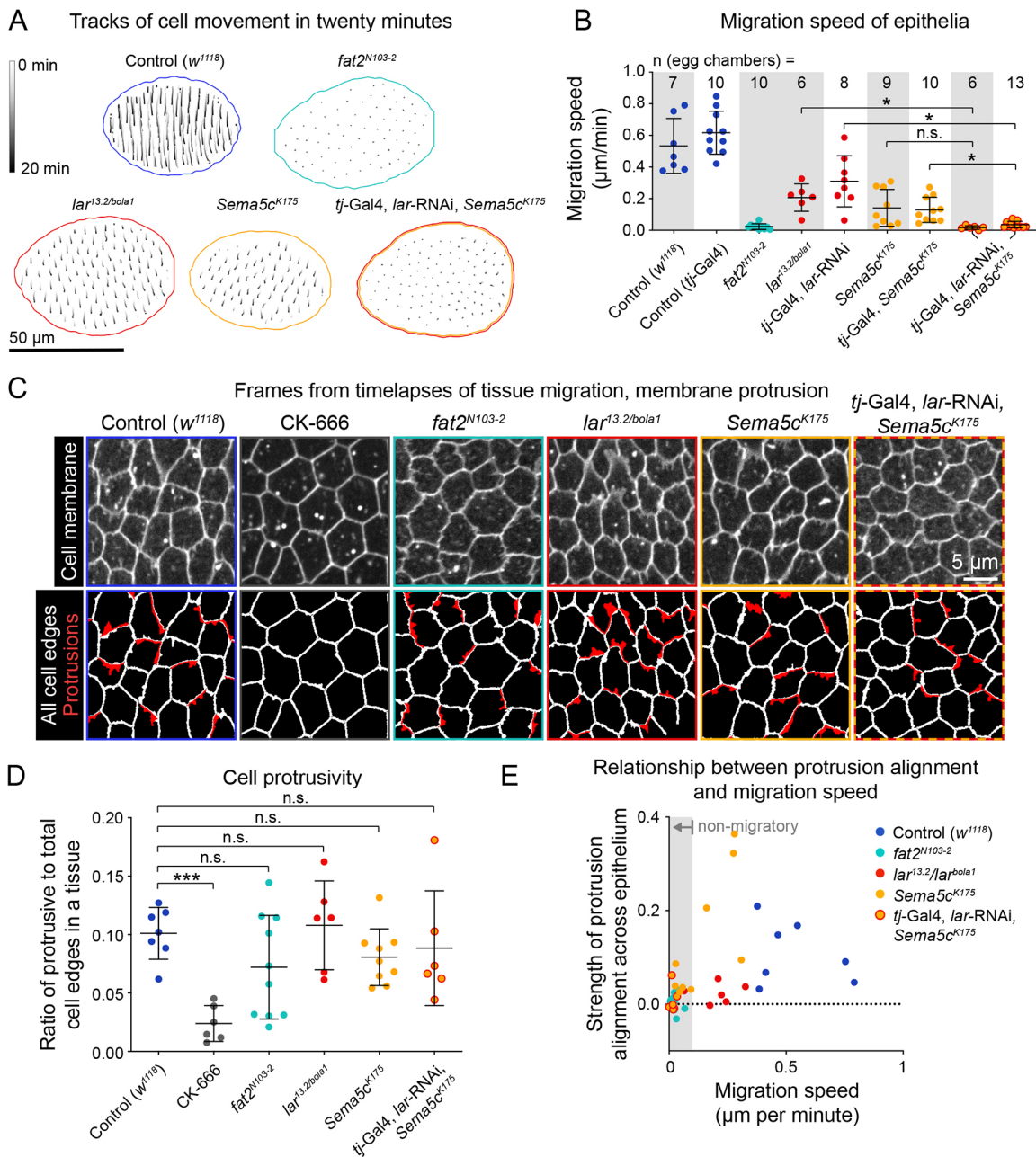


Fig. 7. Lar and Sema5c act in parallel to promote collective migration. (A) Tracks of cell movement over 20 min in individual epithelia. The in-focus tissue region is outlined. (B) Plot of tissue migration speeds. Movies of conditions with white backgrounds on the graph were taken at medial planes through the follicle cells. Movies of conditions with gray backgrounds were taken at the basal surface and used for analysis of membrane protrusion traits in addition to migration speed. Whereas loss of Lar or Sema5c slows migration, simultaneous loss of both Lar and Sema5c stops it entirely. Gray backgrounds: * $P=0.021$; n.s., not significant, $P=0.099$ [Welch's ANOVA ($W(3.000, 14.31)=64.11$, $P<0.0001$) with post-hoc Dunnett's T3 multiple comparisons test]. White backgrounds: * $P=0.011$, * $P=0.025$ (left to right) [Welch's ANOVA ($W(4.000, 14.30)=21.64$, $P<0.0001$) with post-hoc Dunnett's T3 multiple comparisons test]. (C) Frames from timelapse movies used for measurement of migration speed and protrusion traits. Control epithelia treated with CK-666 are used as a non-protrusive control. The top row shows cell membranes labeled with CellMask. The bottom row shows the segmented cell edges and protrusions. Edges categorized as protrusive based on their average lengths of extension are shown in red. (D) Plot of the level of cell protrusivity per epithelium, defined as the ratio of protrusive to total cell edges. Edges are categorized as protrusive if their average length was greater than that of edges in CK-666-treated epithelia. Unlike CK-666 treatment, loss of Fat2, Lar or Sema5c causes only minor changes to the level of cell protrusivity, if any. *** $P=0.0002$; n.s., not significant $P=0.69$, >0.99 , 0.70 , >0.99 (left to right) [Welch's ANOVA ($W(5.000, 16.43)=12.83$, $P<0.0001$) with post-hoc Dunnett's T3 multiple comparisons test]. (E) Plot showing the relationship between migration speed and the strength of protrusion alignment. An alignment of one indicates perfect alignment of all protrusions, and zero indicates either random protrusion orientations or symmetrical protrusion in two opposite directions. The gray region indicates non-migratory epithelia (speed $<0.1 \mu$ m/min). Protrusions of slowly migrating *Sema5c^{K175}* epithelia (but not *lar^{13.2/bola1}* epithelia) are poorly aligned with one another.

(Carmona-Fontaine et al., 2017; Smeets et al., 2016; Zimmermann et al., 2016), which causes cells to polarize away from one another by suppressing protrusion and/or increasing contractility at the point of

contact (Roycroft and Mayor, 2016; Stramer and Mayor, 2017). By localizing Lar and Sema5c to leading edges, Fat2 positions them to enforce trailing edge behavior at the contacting edge of the cell ahead.

Therefore, Fat2 translates a mechanical cue into bi-directional signaling across leading-trailing interfaces to coordinate cell migratory behaviors for collective migration.

MATERIALS AND METHODS

Drosophila sources, care and genetics

The sources and references for all *Drosophila melanogaster* stocks used in this study are listed in [Table S1](#) and the genotypes of the lines corresponding to each figure panel are listed in [Table S2](#). Newly generated plasmids and *Drosophila* strains are available upon request to the corresponding author. *Drosophila* were raised on a diet of cornmeal molasses agar food at 25°C. Experimental females were collected 0–3 days post-eclosion and aged in the presence of males with a diet of the same cornmeal molasses agar supplemented with finely powdered active dry yeast before dissection. In most experiments, they were aged for 2–3 days at 25°C. Higher temperatures were used to increase the expression of Gal4-driven transgenes in some cases, and longer aging times (up to 5 days) were used to obtain more FRT recombination events in some mosaic epithelia. The temperatures and yeasting times used in each experiment are listed in [Table S3](#). Epithelia mosaic for RNAi expression were generated using the Flp-out system with Gal4 expressed under control of a heat-shock promoter. To heat shock, experimental females were aged while undergoing the following 12 h temperature cycle: 1 h 37°C, 1 h 25°C, 1 h 37°C, 9 h 25°C. After 5 cycles (2.5 days), they were then transferred to 29°C and given fresh yeast for an additional 12 h prior to dissection to increase RNAi expression strength and uniformity across clones.

Generation of the Lar-3×GFP line

Endogenous Lar was tagged C-terminally with three enhanced GFP proteins in tandem separated by short linker sequences (3×GFP) using CRISPR following the general approaches described in Gratz et al. (2013, 2014). The same 3×GFP sequence had been used to generate Fat2-3×GFP and Sema5c-3×GFP proteins in previous studies (Barlan et al., 2017; Stedden et al., 2019). The guide RNA target sequence 5'-GCTTCGCTATCGCGTGCACTGG-3' was chosen with flyCRISPR Target Finder (Gratz et al., 2014). The underlined sequence was cloned into the pU6-BbsI-chiRNA plasmid (Gratz et al., 2013; Addgene #45946), the upstream G added for efficient U6-driven expression, and the bold sequence is the adjacent PAM motif. The homologous recombination donor plasmid contained homology arms ~2 kb in length flanking the insertion target site, acquired by amplification of genomic DNA from the y1 Mnos-Cas9.PZH-2A w* (nanos-Cas9) background (Port et al., 2014). The 3×GFP sequence was amplified from the pDsRed-Fat2-3×GFP plasmid (Barlan et al., 2017). A linker with a sequence encoding the amino acids GSGSTVPRARDPPVAT connects the Lar C-terminus with the N-terminus of 3×GFP. Homology arms, linker and 3×GFP DNA fragments were inserted into donor plasmid pDsRed-attP, which contains 3×P3-DsRed flanked by loxP sites for insertion screening and subsequent removal (Gratz et al., 2014). The linker-3×GFP insertion was made immediately before the Lar stop codon. Guide and homologous recombination plasmids were injected by Genetivision in the nanos-Cas9 background, providing a germline Cas9 source. F1 males were screened for 3×P3-DsRed, which is expressed in the eye, and then 3×P3-DsRed was excised by crossing to Cre-expressing flies (MKRS hsFLP/TM6b Cre). Successful insertion was confirmed with genomic DNA sequencing of the lar C-terminus and 3×GFP insertion region following 3×P3-DsRed excision. This insertion strategy leaves a loxP 'scar' downstream of the *lar* protein-coding region.

Egg chamber dissection

Ovaries were dissected into 500 µl of live imaging medium (Schneider's *Drosophila* medium with 15% fetal bovine serum and 200 µg/ml insulin) in a spot plate using one set of Dumont #55 forceps in the experimenters' dominant hand and 1 set of Dumont #5 forceps in the non-dominant hand. A more detailed description and images of this dissection protocol are available in Cetera et al. (2016). Ovarioles were removed from both the ovary and their individual muscle sheaths by pinching the germarium with forceps and pulling anteriorly. For fixed imaging, egg chambers older than

stage 9 were removed prior to fixation. For live imaging, egg chambers older than the egg chamber to be imaged were removed from the ovariole strands by slicing through the adjoining stalk cells with a 27-gauge hypodermic needle. Removal of older egg chambers results in more compression of the younger egg chambers between the slide and the coverslip.

Live imaging sample preparation

Immediately after dissection, ovarioles were transferred to a fresh well of live imaging medium using a p10 pipettor. For samples with membrane staining, CellMask Orange (Thermo Fisher Scientific, Waltham, MA, USA; 1:500) was added and samples incubated for 15 min, and then samples were washed in live imaging medium to remove excess dye before mounting. For samples treated with CK-666, following plasma membrane staining, ovarioles were instead transferred to live imaging medium with 750 µM CK-666 (Millipore Sigma, St Louis, MO, USA) and then mounted immediately after in the same CK-666-containing medium. Samples were mounted along with 51 µm beads on standard glass slides, and covered with 22×22 mm #1.5 coverslips. The beads support the coverslip, controlling the amount of tissue compression. Some compression enables imaging of the basal surface of a field of cells in a single plane, but too much interferes with the migration process. Coverslip edges were sealed with petroleum jelly to prevent evaporation during imaging. Samples were checked for damage using the membrane stain or other available fluorescent markers as indicators, and excluded if damage was present. Slides were imaged for 1 h or less.

EGTA treatment

Egg chambers were dissected into live imaging medium, and then half were transferred into spot plate wells with 250 µl of live imaging medium (the 'control' treatment), and the other half into 250 µl of live imaging medium containing 20 mM EGTA (Thermo Fisher Scientific). They were incubated for 5 or 30 min, depending on the experiment, with wells covered by a slide to slow evaporation, and then fixed and stained with phalloidin as detailed below.

Immunostaining and F-actin staining

After dissection, ovarioles were fixed at room temperature for 15 min in 4% EM-grade formaldehyde in PBT (phosphate-buffered saline with 0.1% Triton X-100 detergent), and then washed three times for 5 min each time in PBT. For antibody staining, egg chambers were incubated in primary antibody (mouse anti-Lar monoclonal, 1:200, or mouse anti-Dlg monoclonal, 1:20; see [Table S1](#) for full details) overnight at 4°C, washed three times for 5 min each time in PBT, and then incubated in secondary antibody (donkey anti-mouse polyclonal, 1:200; [Table S1](#)) for 2–3 h at room temperature. For phalloidin staining, samples were incubated in TRITC-phalloidin (Millipore Sigma, 1:250) for 15 min at room temperature, or with 647 AlexaFluor-phalloidin (Thermo Fisher Scientific, 1:100) for 2–3 h at room temperature. For a more detailed phalloidin staining protocol, see Anderson et al. (2023). Phalloidin and secondary antibody incubations were performed concurrently where applicable. Samples were then washed three times for 5 min each time in PBT and mounted on a slide in a drop (~40 µl) of SlowFade Diamond antifade (Invitrogen), covered in a 22×50 mm #1.5 coverslip sealed with nail polish, and stored at 4°C until imaged. This mounting strategy results in compression of stage 6–7 egg chambers, allowing imaging of the basal surfaces of many cells in a single plane.

Microscopy

All micrograph images collected are of egg chambers at either stage 6 or 7, as assessed by their size and by the size and shape of their oocyte in cross-section. Images were acquired using a Zeiss LSM800 upright laser scanning confocal microscope with either a 40×/1.3 NA EC 386 Plan-NEOFLUAR or 63×/1.4 NA Plan-APOCHROMAT oil immersion objective. The system was controlled with Zen 2.3 Blue acquisition software (Zeiss). Imaging was performed at room temperature. All images and measurements are of a single Z-slice of basal surfaces of the follicle cells unless otherwise noted. Exceptions are Fig. 4B and the bottom rows of Fig. 3A and [Fig. S1A](#), which show cross-sections through the apical-basal axis; Fig. 4D, which show a near-apical plane (the plane of the adherens junctions); and the timelapse

movies used to measure the migration speeds plotted in Fig. 7B on a white background, which were taken at a medial plane through the cells with respect to their apical-basal axis. Unless noted, imaging settings were held constant for all images of the same fluorescent protein shown in the same image panel and any corresponding plot panels, but settings affecting image brightness were optimized separately for each fluorophore when multiple are present in the same panel, or for data shown in separate panels. The exceptions are in Fig. 2A,B and C,D, which were collected with the same imaging settings to enable the comparison in 2E, and Fig. S3G,H, in which Fat2-3×GFP, Lar-3×GFP and Sema5c-3×GFP were imaged and displayed in the same manner to enable comparison of their levels.

Cell tracking and migration speed measurement

Timelapse movies of 20 min in length were acquired of stage 6–7 egg chambers stained with CellMask membrane dye. These were taken at either the medial epithelial plane (used for migration speed measurement only, conditions with white background in Fig. 7B) or the basal plane (for migration speed and protrusion trait measurement, conditions with gray backgrounds). In either case, cells were segmented in each frame using the pretrained ‘cytoplasm’ model in Cellpose (Stringer et al., 2017). Subsequent analysis steps were performed in Python using scikit-image (<https://scikit-image.org/>) and scipy (<https://scipy.org/>) libraries (van der Walt et al., 2014; Virtanen et al., 2020). The gaps between segmented cells were closed with a watershed algorithm seeded by the initial segmented regions. Segmented cells were then tracked by linking regions of high overlap in consecutive frames. Errors in segmentation and tracking were corrected manually using napari (<https://napari.org/>). Migration speed was measured from a 22 μm-wide band of cells around the ‘equator’ of the egg chamber, half-way between the anterior and posterior poles, where linear cell migration speed is fastest in migratory epithelia. The displacement vector as calculated, and these vectors averaged to obtain a vector whose length and direction were used to determine the tissue migration speed and direction. See also ‘Code’ section below.

Measurement of membrane protrusivity and protrusion alignment with migration

Protrusions were identified from timelapse movies of epithelia stained with Cell Mask membrane dye, which yield rich information about protrusion characteristics including their sizes and distributions, and often allow detection of more protrusive activity than is detectable by F-actin labeling. Automated protrusion segmentation was performed using a watershed-based approach, and the average lengths and orientations of these protrusions measured, as described in Williams et al. (2022) and briefly here. Protrusion segmentation and trait measurement were performed in Python using scikit-image and scipy libraries. Following cell segmentation, the region of high membrane fluorescence at the interface between each pair of neighboring cells was segmented. This region includes the cell–cell interface and any protrusions that extend across it from either of the neighboring cells. We then approximated the cell–cell interface position running through this region by drawing the shortest path through the region that connects its bounding vertices. This divides the region into two portions belonging to each of the neighboring cells, which we call ‘edges’.

To obtain a benchmark for the width of non-protrusive cell edges, we identified the average width (area divided by interface length) of edges from CK-666-treated epithelia, which are nearly non-protrusive. Edges from all conditions were considered protrusive if their width (corresponding with their average length of membrane extension from the interface) was greater than that of 98% of those of CK-666-treated epithelia. We then calculated the average cell protrusivity of each epithelium, defined as its ratio of protrusive to total edges.

To measure protrusion polarity, we took the protrusive edges (‘protrusions’), identified their ‘tip’ and ‘base’ as in Williams et al. (2022), and then assigned their orientation as the direction of the vector from base to tip. As a metric for protrusion alignment across an epithelium, we found the dot product of each pair of protrusions present in the same frame, and then took the mean of all dot products. For each protrusion pair, the dot product will be 1 if they have the same orientation, 0 if they are orthogonal to one another, and –1 if they have opposite orientations.

Averaging these for an epithelium would yield an alignment score of 1 if all protrusions were perfectly aligned (high vectorial polarity), but could have a score of zero either if protrusions were randomly oriented (no polarity), or if half pointed in each direction along one axis (high axial polarity, no vectorial polarity). We report alignment of protrusions with one another, rather than with the direction of migration, because this is still meaningful in non-migratory epithelia (whether truly non-migratory or only non-migratory *ex vivo*). In migrating epithelia, protrusion–protrusion alignment and protrusion–migration alignment measurements were highly correlated. See also ‘Code’ section below.

Quantification of Fat2-3×GFP fluorescence at cell–cell interfaces and the basal surface

Egg chambers expressing Fat2-3×GFP were stained with anti-Dlg antibody to label cell edges, stage 6–7 egg chambers were imaged, and the cells were segmented using the pretrained ‘cytoplasm’ model in Cellpose applied to the Dlg channel. Subsequent analysis steps were performed in Python using scikit-image and scipy libraries. Gaps between segmented cells were closed with a watershed algorithm seeded by the initial segmented regions, and segmentation errors were then manually corrected using napari. Mean fluorescence intensity was calculated at cell–cell interfaces (boundaries between segmented cells dilated by 10 pixels) and the entire in-focus basal surface. See also ‘Code’ section below.

Measurement of fluorescence intensity at leading–trailing interfaces

Leading–trailing interface regions were annotated by hand based on phalloidin staining using Fiji (ImageJ; Schindelin et al., 2012, 2015) as follows: 10 pixel-wide segmented lines were drawn along leading–trailing interfaces and then the mean fluorescence intensity across those interfaces was calculated. In experiments with non-mosaic epithelia, at least ten leading–trailing interfaces were measured. For more information about measurement in mosaic epithelia, see the next section. Note that no correction was performed for background fluorescence, so the proportional relationship between fluorescence intensity measurements should not be interpreted as corresponding directly to the proportional relationship between protein levels.

Analysis of localizing interactions and their cell autonomy

Analysis of protein localization in genetically mosaic epithelia was used to disentangle cell- and interface-scale protein-localizing interactions from the tissue-wide effects of genotype on planar polarity and migration. It was also used to determine the cell autonomy of localizing interactions. Interpretations of the cell autonomy of effects on the localization of Lar or Sema5c were made based on the much greater enrichment of Lar and Sema5c at leading edges than at trailing edges in normal circumstances (Barlan et al., 2017; Stedden et al., 2019) (see Fig. 1C). In epithelia mosaic, for a loss-of-function mutation (generated using the Flp/FRT system), cells with the chromosome containing the wild-type allele were marked with a nucleus-enriched fluorophore, and ‘control’ cells include both homozygous wild-type and heterozygous cells. In epithelia mosaic for RNAi expression (generated using the Flp-out system), RNAi-expressing cells were marked with a nucleus-enriched fluorophore. F-actin staining with AlexaFluor 647–phalloidin was used to visually assess whether epithelia were planar-polarized and migratory (based on stress fiber alignment across the epithelium), their migration direction (based on the orientation of leading edge protrusions), and to check for regions of tissue damage that could otherwise be misinterpreted as genetic clones. Egg chambers were included in subsequent analysis if they were within stage 6–7, had planar-polarized actin stress fibers, and had both control and mutant or RNAi-expressing cells in view with at least three leading–trailing interfaces between cells of each genotype combination. For measurement of fluorescence levels at leading–trailing interfaces between pairs of cells of each genotype combination, mean fluorescence intensity at individual leading–trailing interfaces was measured as described in the previous section, with all leading–trailing interfaces at genotype boundaries, and a similar number of clone-internal ones, included. Plots show intensities rescaled per sample, such that the mean fluorescence intensity at leading–trailing interfaces between control

cells is equal to 1. For comparison of fluorescence levels at leading-trailing versus side interfaces, the mean fluorescence intensity at leading-trailing and side interfaces between pairs of control cells and between pairs of mutant or RNAi-expressing cells was measured as described in the previous section except that tricellular junctions were not included in the interface regions. Plots show intensities rescaled such that the mean fluorescence intensity at side interfaces between control cells is equal to 1. Plots were generated using GraphPad Prism 9.

Plotting of protein intensity along an 'unrolled' cell perimeter

Plots of 'unrolled' cell perimeters were used to display the distributions of Fat2, Lar and GrabFP-A^{Int} fluorescence around cell perimeters and the correspondence between those distributions. 10 pixel-wide segmented lines were drawn around the perimeter of cells in Fiji, and fluorescence intensities measured. Using Python, intensities were rescaled for ease of comparison and plotted. Specifically, Fat2-3×GFP and anti-Lar intensities were rescaled such that they had a range of 0 to 1 in the control dataset. GrabFP-A^{Int} was rescaled proportionally to Fat2-3×GFP.

FRAP analysis of protein exchange at leading-trailing interfaces

Photobleaching was performed on samples mounted and imaged as described in previous sections using the timed bleaching tool in Zen Blue. Focusing at the basal surface plane, leading-trailing interface regions between two vertices, excluding those vertices, were selected for bleaching. Lar-3×GFP, *fat2*^{N103-2} and Sema5c-3×GFP, *fat2*^{N103-2} epithelia were non-migratory and lacked planar polarity, so any interfaces were used. Up to four interfaces were bleached per egg chamber, always from non-neighboring cells. Two frames were acquired before bleaching, bleaching was performed once, and then timelapse acquisition continued for a total of either 8 min (at 10 s/frame) or 30 min (at 30 s/frame). Bleached interfaces were excluded from analysis if the majority of the interface length was not bleached, the bleached region encompassed a cell vertex, or the bleached interface was not in view throughout the timelapse. Fluorescence intensity measurements were made using Fiji. Rectangular regions were drawn around the bleached interfaces and the same number of non-bleached interfaces, the positions of these regions were translated in each time point as needed to follow interface movement, and the mean intensity of each was measured. Subsequent analysis and plotting were performed using Python. The mean fluorescence per time point was calculated separately for bleached and unbleached regions, and the mean of the unbleached regions used to rescale the bleached regions to correct for the effects of progressive photobleaching and region selection inaccuracy. The bleach-corrected values were then rescaled so that the time point just before bleaching had a value of one, and the time point just after bleaching zero. Standard deviations were calculated for each time point from the mean intensities of individual bleached regions after they were rescaled in the same manner. For calculation of the time to half recovery, single exponential curves of the form $I(t)=A(1-e^{-t/\tau})$ were fit to data from individual interfaces, where I is fluorescence intensity, t is time, and the parameters A (the immobile fraction) and τ are fit. Time to half recovery ($\tau_{1/2}$, $\frac{\ln(0.5)}{-\tau}$) was then calculated for each interface. In each of the Sema5c-3×GFP and Lar-3×GFP *fat2*^{N103-2} datasets there was one interface with a time to half recovery that was higher than the others by 3–4 orders of magnitude, and these were excluded.

Movie generation

For timelapse movies (but not analysis) of FRAP at cell–cell interfaces (Movies 1, 2), bleach correction was performed on the full tissue timelapse using the 'simple ratio' method in ImageJ prior to cropping and movie generation, and the cropped region was moved to follow the interface. For all movies, margins, scale bars and text labels were first added to TIF image stacks using ImageJ or Adobe Illustrator 2021, and then the files exported from ImageJ as uncompressed AVI files. These were encoded as 1080 p30 MP4 files with H.264 (×264) video encoder using HandBrake 1.4 (<https://handbrake.fr/>).

Reproducibility and statistical analysis

Two or more biological replicates were performed for each experiment, with each containing egg chambers pooled from multiple flies, and results

confirmed to be qualitatively consistent between them. Visibly damaged egg chambers were excluded from all analyses. No randomization of treatment groups was performed, and experiments were not performed with blinding. Sample sizes were not predetermined using a statistical method. The number of egg chambers, interfaces and/or filopodia (n) analyzed for each experiment can be found in the associated figure or figure legend. Statistical tests performed and their significance can also be found in figures or figure legends. An alpha of 0.05 was used to determine significance in all cases, but we have also attempted to plot data distributions in ways that allow the reader to weigh their similarities and differences for themselves. Statistical testing was conducted using GraphPad Prism 9. Based on visual inspection, all datasets appeared normally distributed, and statistical tests assuming normalcy were used throughout. All t -tests were two-tailed. A one-way ANOVA was used when more than two conditions were compared. A repeated measures one-way ANOVA was used for analysis of genetic mosaic epithelia, in which multiple genetic conditions were present in the same tissue. Welch's corrections were performed and Dunnett's T3 multiple comparison tests used for datasets in which the variance did not appear consistent between conditions (indicated in figure legends). Otherwise, post-hoc Tukey's multiple comparison tests were used. Initial and post-hoc multiple comparisons testing was conducted on all data present in the corresponding plots with two exceptions: in Fig. 3C, only data including the same fluorophore were compared, and in Fig. 7B, data from conditions with gray and white background shading were collected and analyzed separately.

Code

Code used in data analysis is described where applicable in the previous sections and is available at https://github.com/a9w/epithelial_migration_signaling.

Acknowledgements

We thank members of the Horne-Badovinac and Munro Labs, Michael Glotzer, Ellie Heckscher for discussion, Seth Donoughe for image analysis advice, and the University of Chicago DNA Sequencing Facility for sequencing data acquisition.

Competing interests

The authors declare no competing or financial interests.

Author contributions

Conceptualization: A.M.W., S.H.; Software: A.M.W.; Formal analysis: A.M.W.; Investigation: A.M.W.; Writing - original draft: A.M.W.; Writing - review & editing: A.M.W., S.H.; Supervision: S.H.; Funding acquisition: S.H.

Funding

This study was supported by the National Institutes of Health (NIH) under grants R01 GM126047 and R35 GM148485 to S.H.B. and T32 HD055164 to A.M.W. Deposited in PMC for release after 12 months.

Data availability

Image and numerical data and plasmid maps generated in this study are available at <https://doi.org/10.6084/m9.figshare.23564223>.

Peer review history

The peer review history is available online at <https://journals.biologists.com/jcs/lookup/doi/10.1242/jcs.261173.reviewer-comments.pdf>

References

- Alto, L. T. and Terman, J. R. (2017). Semaphorins and their signaling mechanisms. *Methods Mol. Biol.* **1493**, 1–25. doi:10.1007/978-1-4939-6448-2_1
- Anderson, M. T., Sherrard, K. and Horne-Badovinac, S. (2023). Optimized fixation and phalloidin staining of basally localized F-Actin networks. In *Drosophila Oogenesis: Methods and Protocols, Methods in Molecular Biology*, Vol. 2626 (ed. M. S. Giedt and T. L. Tootle), pp. 179–191, Springer.
- Barlan, K., Cetera, M. and Horne-Badovinac, S. (2017). Fat2 and lar define a basally localized planar signaling system controlling collective cell migration. *Dev. Cell* **40**, 467–477.e5. doi:10.1016/j.devcel.2017.02.003
- Bateman, J., Reddy, R. S., Saito, H. and Van Vector, D. (2001). The receptor tyrosine phosphatase Dlar and integrins organize actin filaments in the *Drosophila* follicular epithelium. *Curr. Biol.* **11**, 1317–1327. doi:10.1016/S0960-9822(01)00420-1
- Brasch, J., Goodman, K. M., Noble, A. J., Rapp, M., Manneppalli, S., Bahna, F., Dandey, V. P., Bepler, T., Berger, B., Maniatis, T. et al. (2019). Visualization

- of clustered protocadherin neuronal self-recognition complexes. *Nature* **569**, 280–283. doi:10.1038/s41586-019-1089-3
- Carmona-Fontaine, C., Matthews, H. K., Kuriyama, S., Moreno, M., Dunn, G. A., Parsons, M., Stern, C. D. and Mayor, R.** (2017). Contact inhibition of locomotion in vivo controls neural crest directional migration. *Nature* **456**, 957–961. doi:10.1038/nature07441
- Cetera, M., Ramirez-San Juan, G. R., Oakes, P. W., Lewellyn, L., Fairchild, M. J., Tanentzapf, G., Gardel, M. L. and Horne-Badovinac, S.** (2014). Epithelial rotation promotes the global alignment of contractile actin bundles during *Drosophila* egg chamber elongation. *Nat. Commun.* **5**, 5511. doi:10.1038/ncomms6511
- Cetera, M., Lewellyn, L. and Horne-Badovinac, S.** (2016). Cultivation and live imaging of *Drosophila* ovaries. In *Drosophila: Methods and Protocols, Methods in Molecular Biology*, Vol. 1478 (ed. C. Dahmann), pp. 215–226, Springer.
- Crest, J., Diz-Muñoz, A., Chen, D.-Y., Fletcher, D. A. and Bilder, D.** (2017). Organ sculpting by patterned extracellular matrix stiffness. *eLife* **6**, e24958. doi:10.7554/eLife.24958
- Das, T., Safferling, K., Rausch, S., Grabe, N., Boehm, H. and Spatz, J. P.** (2015). A molecular mechanotransduction pathway regulates collective migration of epithelial cells. *Nat. Cell Biol.* **17**, 276–287. doi:10.1038/ncb3115
- Friedl, P. and Gilmour, D.** (2009). Collective cell migration in morphogenesis, regeneration and cancer. *Nat. Rev. Mol. Cell Biol.* **10**, 445–457. doi:10.1038/nrm2720
- Gratz, S. J., Cummings, A. M., Nguyen, J. N., Hamm, D. C., Donohue, L. K., Harrison, M. M., Wildonger, J. and O'Connor-Giles, K. M.** (2013). Genome engineering of *Drosophila* with the CRISPR RNA-guided Cas9 nuclease. *Genetics* **194**, 1029–1035. doi:10.1534/genetics.113.152710
- Gratz, S. J., Ukken, F. P., Rubinstein, C. D., Thiede, G., Donohue, L. K., Cummings, A. M. and O'Connor-Giles, K. M.** (2014). Highly specific and efficient CRISPR/Cas9-catalyzed homology-directed repair in *Drosophila*. *Genetics* **196**, 961–971. doi:10.1534/genetics.113.160713
- Gupta, S. and Yap, A. S.** (2021). How adherens junctions move cells during collective migration. *Fac. Rev.* **10**, 56. doi:10.12703/r/10-56
- Gutzeit, H. O., Eberhardt, W. and Gratwohl, E.** (1991). Laminin and basement membrane-associated microfilaments in wild-type and mutant *Drosophila* ovarian follicles. *J. Cell Sci.* **100**, 781–788. doi:10.1242/jcs.100.4.781
- Haigo, S. L. and Bilder, D.** (2011). Global Tissue Revolutions in a morphogenetic movement controlling elongation. *Science* **331**, 1071–1074. doi:10.1126/science.1199424
- Harmansa, S., Albores, I., Bieli, D., Caussin, E. and Affolter, M.** (2017). A nanobody-based toolset to investigate the role of protein localization and dispersal in *Drosophila*. *eLife* **6**, e22549. doi:10.7554/eLife.22549
- Hayer, A., Shao, L., Chung, M., Joubert, L. M., Yang, H. W., Tsai, F.-C., Bisaria, A., Betzig, E. and Meyer, T.** (2016). Engulfed cadherin fingers are polarized junctional structures between collectively migrating endothelial cells. *Nat. Cell Biol.* **18**, 1311–1323. doi:10.1038/ncb3438
- Hung, R.-J. and Terman, J. R.** (2011). Extracellular inhibitors, repellents, and semaphorin / plexin / MICAL-mediated actin filament disassembly. *Cytoskeleton* **68**, 415–433.
- Isabella, A. J. and Horne-Badovinac, S.** (2016). Rab10-mediated secretion synergizes with tissue movement to build a polarized basement membrane architecture for organ morphogenesis. *Dev. Cell* **38**, 47–60. doi:10.1016/j.devcel.2016.06.009
- Jain, S., Cachoux, V. M. L., Narayana, G. H. N. S., de Beco, S., D'Alessandro, J., Cellerin, V., Chen, T., Heuzé, M. L., Marcq, P., Mège, R.-M. et al.** (2020). The role of single-cell mechanical behaviour and polarity in driving collective cell migration. *Nat. Phys.* **16**, 802–809. doi:10.1038/s41567-020-0875-z
- Kim, S. A., Tai, C.-Y., Mok, L.-P., Mosser, E. A. and Schuman, E. M.** (2011). Calcium-dependent dynamics of cadherin interactions at cell–cell junctions. *Proc. Natl Acad. Sci. USA* **108**, 9857–9862. doi:10.1073/pnas.1019003108
- Krdnja, D., Marjou, F. E., Guirao, B., Richon, S., Leroy, O., Bellaiche, Y., Hannezo, E. and Vignjevic, D. M.** (2019). Active cell migration is critical for steady-state epithelial turnover in the gut. *Science* **365**, 705–710. doi:10.1126/science.aau3429
- Nagar, B., Overduin, M., Ikura, M. and Rini, J. M.** (1996). Structural basis of calcium-induced E-cadherin rigidification and dimerization. *Nature* **380**, 360–364. doi:10.1038/380360a0
- Port, F., Chen, H.-M., Lee, T. and Bullock, S. L.** (2014). Optimized CRISPR/Cas tools for efficient germline and somatic genome engineering in *Drosophila*. *Proc. Natl Acad. Sci. USA* **111**, E2967–E2976. doi:10.1073/pnas.1405500111
- Roberto, G. M. and Emery, G.** (2022). Directing with restraint: Mechanisms of protrusion restriction in collective cell migrations. *Semin. Cell Dev. Biol.* **129**, 75–81. doi:10.1016/j.semdcb.2022.03.037
- Rorh, P.** (2012). Fellow travellers: Emergent properties of collective cell migration. *EMBO Rep.* **13**, 984–991. doi:10.1038/embor.2012.149
- Roycroft, A. and Mayor, R.** (2016). Molecular basis of contact inhibition of locomotion. *Cell. Mol. Life Sci.* **73**, 1119–1130. doi:10.1007/s00018-015-2090-0
- Schindelin, J., Arganda-Carreras, I., Frise, E., Kaynig, V., Longair, M., Pietzsch, T., Preibisch, S., Rueden, C., Saalfeld, S., Schmid, S. et al.** (2012). Fiji: An open-source platform for biological-image analysis. *Nat. Methods* **9**, 676–682. doi:10.1038/nmeth.2019
- Schindelin, J., Rueden, C. T., Hiner, M. C. and Eliceiri, K. W.** (2015). The ImageJ ecosystem: An open platform for biomedical image analysis. *Mol. Reprod. Dev.* **82**, 518–529. doi:10.1002/mrd.22489
- Shaw, T. J. and Martin, P.** (2016). Wound repair: A showcase for cell plasticity and migration. *Curr. Opin. Cell Biol.* **42**, 29–37. doi:10.1016/j.cob.2016.04.001
- Sherrard, K. M., Cetera, M. and Horne-Badovinac, S.** (2021). DAAM mediates the assembly of long-lived, treadmill stress fibers in collectively migrating epithelial cells in *Drosophila*. *eLife* **10**, e72881. doi:10.7554/eLife.72881
- Smeets, B., Alert, R., Pešek, J., Pagonabarraga, I., Ramon, H. and Vincent, R.** (2016). Emergent structures and dynamics of cell colonies by contact inhibition of locomotion. *Proc. Natl Acad. Sci. USA* **113**, 14621–14626. doi:10.1073/pnas.1521151113
- Soans, K. G., Ramos, A. P., Sidhaye, J., Krishna, A., Solomatina, A., Hoffmann, K. B., Schlüßler, R., Guck, J., Sbalzarini, I. F., Modes, C. D. et al.** (2022). Collective cell migration during optic cup formation features changing cell-matrix interactions linked to matrix topology. *Curr. Biol.* **32**, 4817–4831.e9. doi:10.1016/j.cub.2022.09.034
- Squarr, A. J., Brinkmann, K., Chen, B., Steinbacher, T., Ebneth, K., Rosen, M. K. and Bogdan, S.** (2016). Fat2 acts through the WAVE regulatory complex to drive collective cell migration during tissue rotation. *J. Cell Biol.* **212**, 591–603. doi:10.1083/jcb.201508081
- Stahley, S. N., Basta, L. P., Sharan, R. and Devenport, D.** (2021). Celsr1 adhesive interactions mediate the asymmetric organization of planar polarity complexes. *eLife* **10**, e62097. doi:10.7554/eLife.62097
- Stedden, C. G., Menegas, W., Zajac, A. L., Williams, A. M., Cheng, S., Özkan, E. and Horne-Badovinac, S.** (2019). Planar-polarized Semaphorin-5c and Plexin A promote the collective migration of epithelial cells in *Drosophila*. *Curr. Biol.* **29**, 908–920.e6.
- Stock, J. and Pauli, A.** (2021). Self-organized cell migration across scales—from single cell movement to tissue formation. *Development* **148**, dev191767. doi:10.1242/dev.191767
- Stramer, B. and Mayor, R.** (2017). Mechanisms and in vivo functions of contact inhibition of locomotion. *Nat. Rev. Mol. Cell Biol.* **18**, 43–55. doi:10.1038/nrm.2016.118
- Stringer, C., Wang, T., Michaelos, M. and Pachitariu, M.** (2017). Cellpose: a generalist algorithm for cellular segmentation. *Nat. Methods* **18**, 100–106. doi:10.1038/s41592-020-01018-x
- Theveneau, E. and Mayor, R.** (2013). Collective cell migration of epithelial and mesenchymal cells. *Cell. Mol. Life Sci.* **70**, 3481–3492. doi:10.1007/s00018-012-1251-7
- Truong Quang, B.-A., Mani, M., Markova, O., Lecuit, T. and Lenne, P.-F.** (2013). Principles of E-Cadherin supramolecular organization in vivo. *Curr. Biol.* **23**, 2197–2207. doi:10.1016/j.cub.2013.09.015
- Tsukasaki, Y., Miyazaki, N., Matsumoto, A., Nagae, S., Yonemura, S., Tanoue, T., Iwasaki, K. and Takeichi, M.** (2014). Giant cadherins Fat and Dachsous self-bend to organize properly spaced intercellular junctions. *Proc. Natl Acad. Sci. USA* **111**, 16011–16016. doi:10.1073/pnas.1418990111
- van der Walt, S., Schönberger, J. L., Nunez-Iglesias, J., Boulogne, F., Warner, J. D., Yager, N., Guillard, E. and Yu, T.** (2014). Scikit-image: Image processing in Python. *PeerJ* **2**, e453. doi:10.7717/peerj.453
- Venhuizen, J.-H. and Zegers, M. M.** (2017). Making heads or tails of it: Cell–cell adhesion in cellular and supracellular polarity in collective migration. *Cold Spring Harbor Perspect. Biol.* **9**, a027854.
- Verhagen, M. G. and Pasterkamp, R. J.** (2020). Axon guidance: Semaphorin/neuropilin/plexin signaling. In *Cellular Migration and Formation of Axons and Dendrites*, pp. 109–122. Elsevier.
- Viktorinová, I. and Dahmann, C.** (2013). Microtubule polarity predicts direction of egg chamber rotation in *Drosophila*. *Curr. Biol.* **23**, 1472–1477. doi:10.1016/j.cub.2013.06.014
- Viktorinová, I., König, T., Schlichting, K. and Dahmann, C.** (2009). The cadherin Fat2 is required for planar cell polarity in the *Drosophila* ovary. *Development* **136**, 4123–4132. doi:10.1242/dev.039099
- Virtanen, P., Gommers, R., Oliphant, T. E., Haberland, M., Reddy, T., Cournapeau, D., Burovski, E., Peterson, P., Weckesser, W., Bright, J. et al.** (2020). SciPy 1.0: Fundamental algorithms for scientific computing in Python. *Nat. Methods* **17**, 261–272. doi:10.1038/s41592-019-0686-2
- Williams, A. M., Donoughe, S., Munro, E. and Horne-Badovinac, S.** (2022). Fat2 polarizes the WAVE complex in trans to align cell protrusions for collective migration. *eLife* **11**, e78343. doi:10.7554/eLife.78343
- Wu, Y., Kanchanawong, P. and Zaidel-Bar, R.** (2015). Actin-delimited adhesion-independent clustering of E-Cadherin forms the nanoscale building blocks of adherens junctions. *Dev. Cell* **32**, 139–154. doi:10.1016/j.devcel.2014.12.003
- Zimmermann, J., Camley, B. A., Rappel, W.-J. and Levine, H.** (2016). Contact inhibition of locomotion determines cell–cell and cell–substrate forces in tissues. *Proc. Natl Acad. Sci. USA* **113**, 2660–2665. doi:10.1073/pnas.1522330113

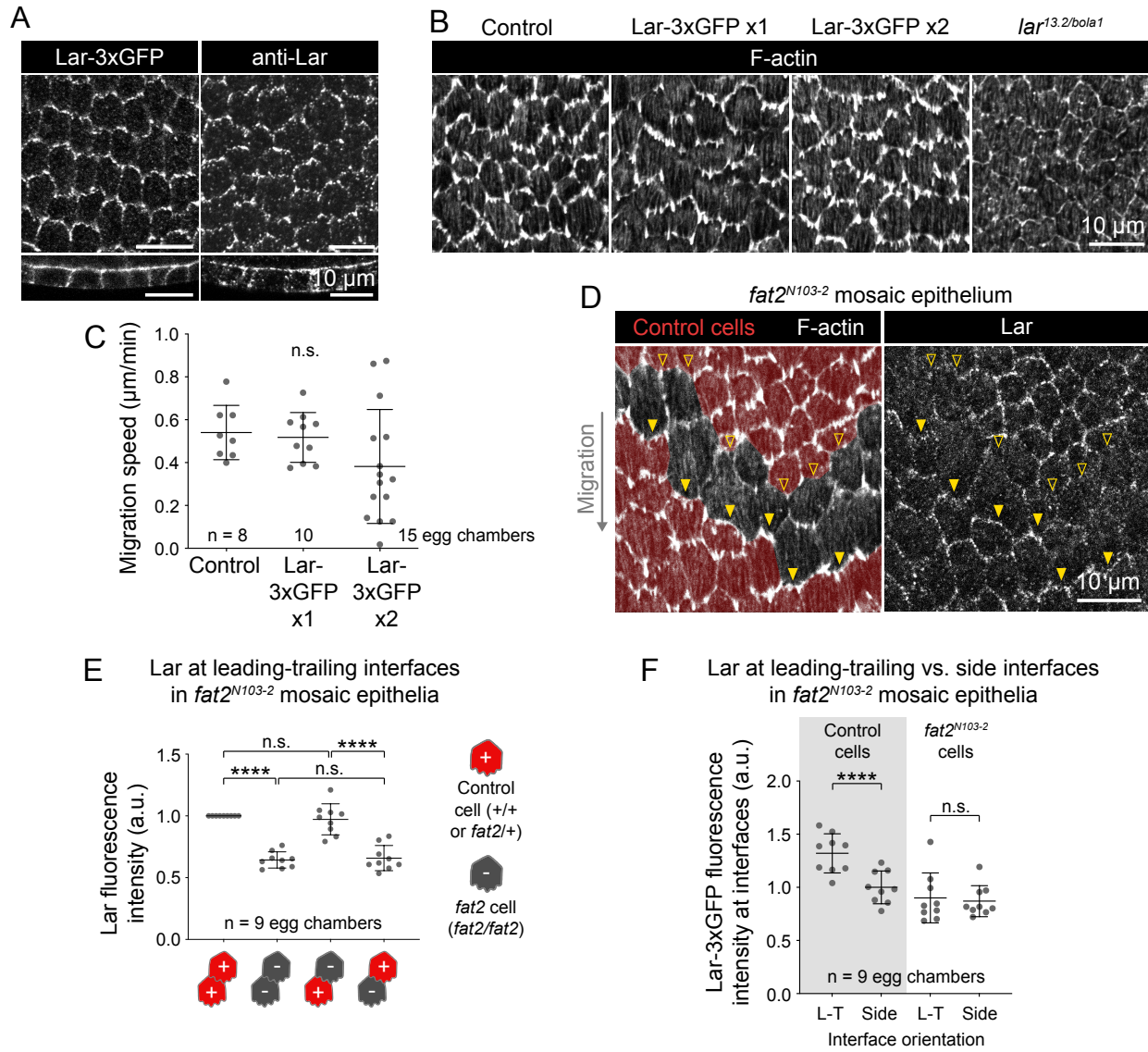


Fig. S1. Lar remains largely functional with an endogenous 3xGFP tag. **A**, Images showing Lar's distribution at the basal surface (top row) or in cross-section (bottom row) as detected using either Lar-3xGFP or a Lar antibody. Lar localization patterns are similar between the two markers. **B**, Images showing F-actin (phalloidin) structures at the basal surface in epithelia with wild-type Lar, one or two Lar-3xGFP alleles, or with no Lar expression. F-actin protrusions appear normal in epithelia expressing Lar-3xGFP, in contrast to the reduced F-actin protrusions in epithelia without Lar. **C**, Plot of follicle cell migration speeds in control epithelia or epithelia with one or two Lar-3xGFP copies. Average migration speeds are similar to controls when one copy of Lar-3xGFP is present, but they are more variable and possibly slower in Lar-3xGFP homozygotes. Welch's ANOVA ($W(2.00, 19.01)=1.92$, $p=0.17$). **D**, Images of a *fat2^{N103-2}* mosaic epithelium expressing Lar-3xGFP, with F-actin stained using phalloidin. Control cells are pseudocolored based on a genetically-encoded fluorescent marker. Filled arrows indicate the leading edges of *fat2^{N103-2}* cells behind control cells, hollow arrows indicate the leading edges of control cells behind *fat2^{N103-2}* cells. **E**, Plot of Lar-3xGFP fluorescence intensity at leading-trailing interfaces between different combinations of control and *fat2^{N103-2}* cells. Lar-3xGFP enrichment is reduced at leading edges of cells of any genotype behind *fat2^{N103-2}* cells, showing that the trans interaction between Fat2 and Lar that was identified using Lar antibody staining (Barlan et al., 2017) is preserved with Lar-3xGFP. Repeated measures one-way ANOVA ($F(3, 24)=60.38$, $p<0.0001$ with post-hoc Tukey's test; n.s. (left to right) $p=0.66$, 0.96 , **** $p<0.0001$). **F**, Plot of Lar-3xGFP fluorescence intensity at leading-trailing (L-T) or side interfaces in *fat2^{N103-2}* mosaic epithelia. Within *fat2^{N103-2}* cell clones, Lar-3xGFP levels at leading-trailing interface are reduced such that they are no longer higher than at side interfaces. Repeated measures one-way ANOVA ($F(3, 24)=35.62$, $p<0.0001$ with post-hoc Tukey's test; n.s. $p=0.92$, **** $p<0.0001$).

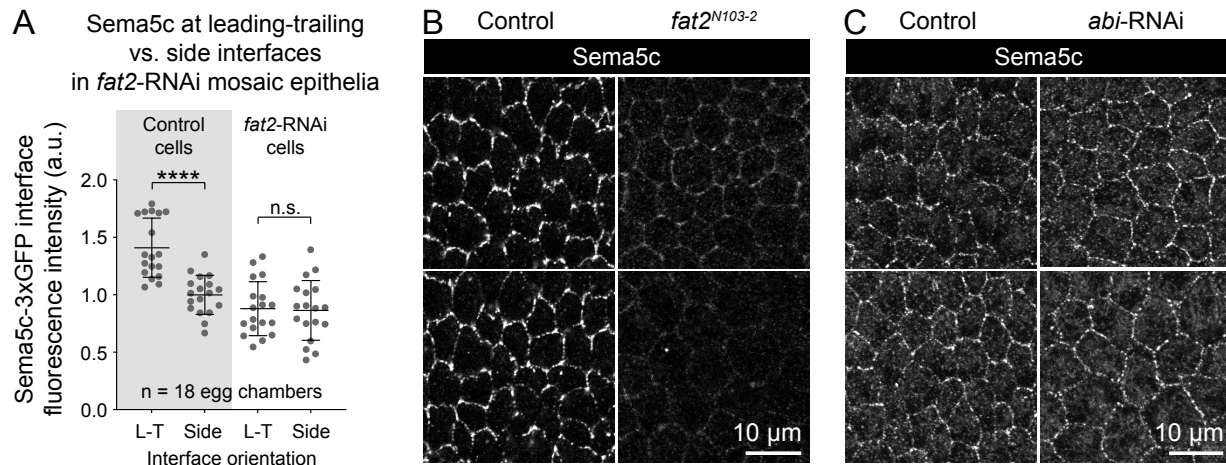


Fig. S2. Fat2 concentrates Sema5c at leading edges in a manner independent of the WAVE complex or protrusions. **A**, Plot of Sema5c-3xGFP fluorescence intensity at leading-trailing (L-T) or side interfaces in *fat2*-RNAi mosaic epithelia. Within *fat2*-RNAi cell clones, Sema5c-3xGFP levels at leading-trailing interface are reduced such that they are no longer higher than at side interfaces. Repeated measures one-way ANOVA ($F(3, 51)=88.51$, $p<0.0001$ with post-hoc Tukey's test; n.s. $p=0.98$, **** $p<0.0001$). Related to Fig. 2A,B. **B**, Images of Sema5c-3xGFP at the basal surfaces of control and *fat2*^{N103-2} epithelia. Sema5c-3xGFP's levels are reduced at cell-cell interfaces in *fat2*^{N103-2} epithelia. **C**, Images of Sema5c-3xGFP at the basal surfaces of control epithelia and ones expressing RNAi against WAVE complex subunit Abi. Tissue-wide planar polarity is lost in *abi*-RNAi-expressing epithelia, but Sema5c-3xGFP remains enriched at interfaces.

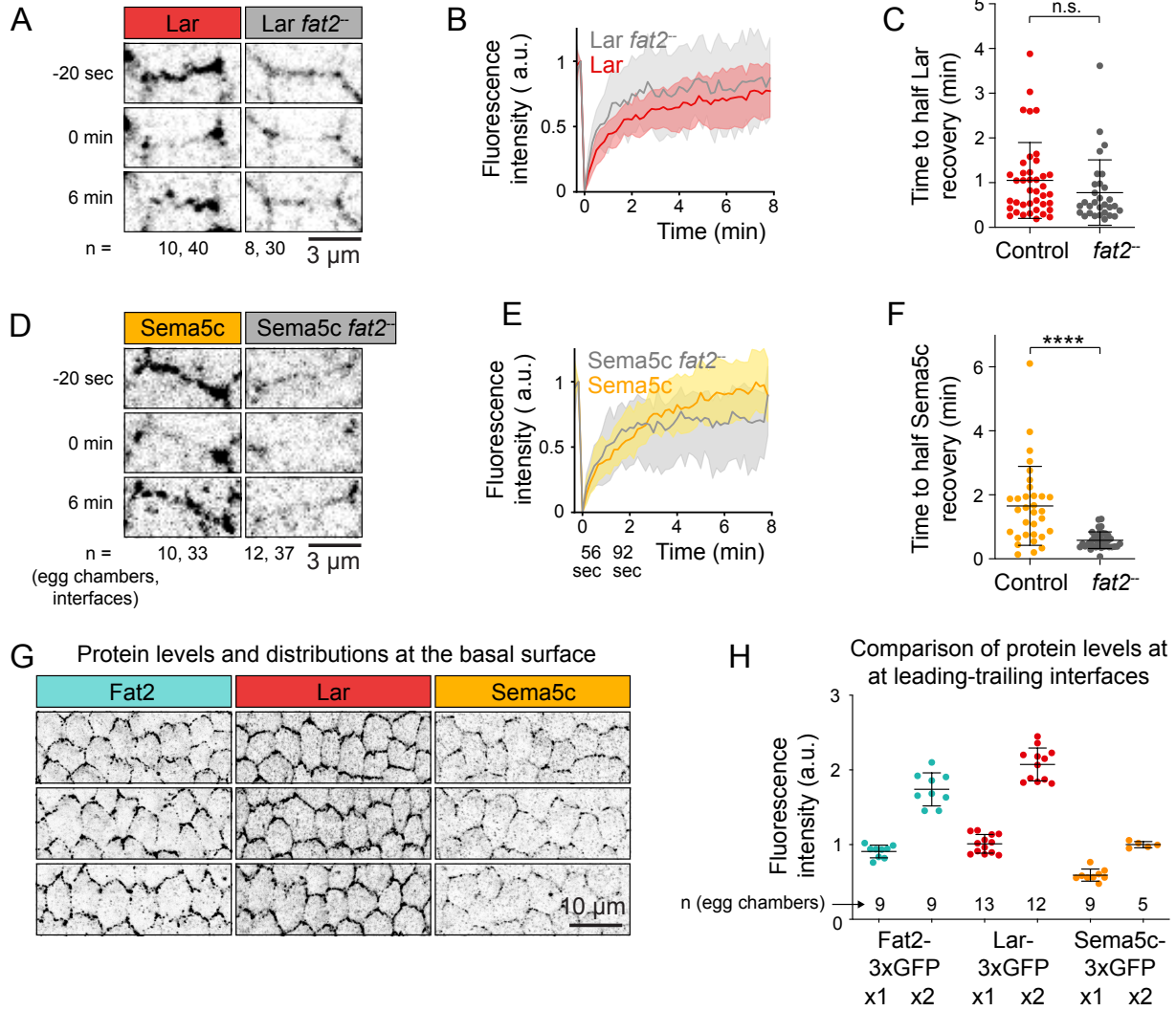


Fig. S3. FRAP measurement of Fat2's effect on Lar and Sema5c turnover at leading-trailing interfaces. **A,D**, Images of Lar-3xGFP and Sema5c-3xGFP at individual leading-trailing interfaces (control) or non-migratory (*fat2*⁻) cell-cell interfaces before, immediately after, and 6 minutes after photobleaching. Control images are reproduced from Fig. 6. **B,E**, Plots showing recovery of Lar-3xGFP and Sema5c-3xGFP fluorescence intensity to leading-trailing (control) or non-migratory (*fat2*⁻) cell-cell interfaces over 8 minutes following photobleaching, exemplified in (A,D). Solid lines and filled regions show mean \pm SD. Control curves are reproduced from Fig. 6. **C,F**, Plots of the time to half fluorescence recovery of Lar-3xGFP and Sema5c-3xGFP, calculated by fitting single exponential equations to data in (B,E). Lar-3xGFP half re-recovery time showed an average decrease in *fat2*^{N103-2} epithelia that was not statistically significant. Welch's t-test, $p=0.15$. Sema5c-3xGFP half recovery is significantly faster in the absence of Fat2 due to changes in both the measured recovery rate and total percent recovery. Welch's t-test, <0.0001 . **G**, Images of Fat2-3xGFP, Lar-3xGFP, and Sema5c-3xGFP at the basal surfaces of rows of cells from multiple epithelia acquired and displayed using uniform settings. **H**, Plot comparing the levels of Fat2-3xGFP, Lar-3xGFP, and Sema5c-3xGFP at leading-trailing interfaces, expressed in two copies or with a wild-type allele. Fluorescence intensity at leading-trailing interfaces differed between the three proteins, with Sema5c-3xGFP fluorescence approximately half that of Fat2-3xGFP or Lar-3xGFP. No correction for background fluorescence was performed.

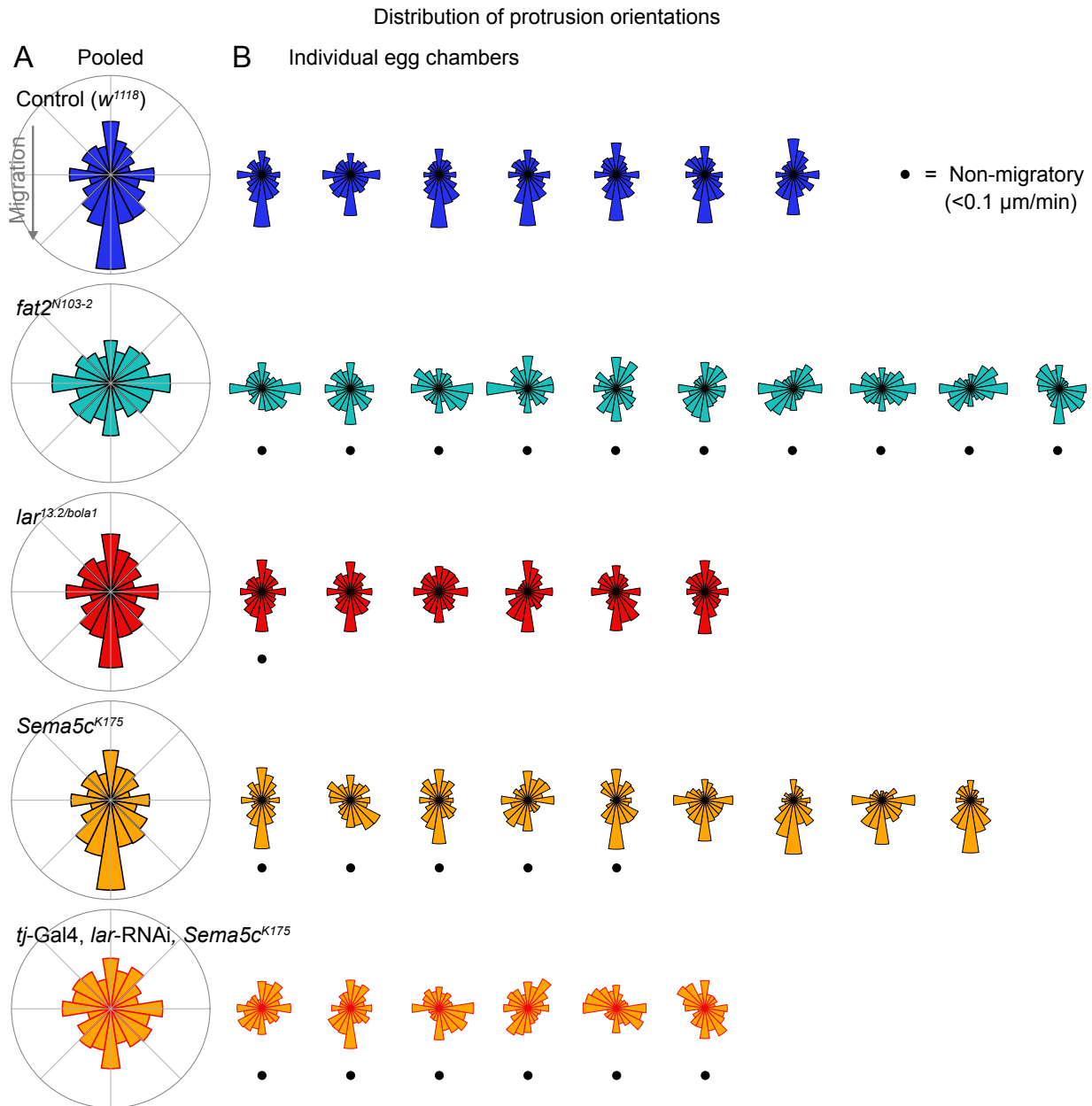


Fig. S4. Loss of either Fat2, Lar, or Sema5c have different effects on the polarity of membrane protrusions. A,B, Po-lar histograms showing the distribution of protrusion orientations in epithelia pooled by genotype (A) or plotted individually (B). In (B), dots under histograms indicate that the epithelium was not migrating (speed $<0.1 \mu\text{m}/\text{min}$). Anterior is left, posterior is right, and data has been flipped vertically as needed such that the migration direction (where applicable) is downwards. *lar^{13.2/bola1}* epithelia have excess rearwards protrusions, and removal of both Lar and Sema5c causes protrusions to be unpolarized, as is seen upon loss of Fat2.

Table S1. Resources and reagents

Reagent type (species) or resource	Designation	Source or reference	Identifiers	Additional information
gene (<i>Drosophila melanogaster</i>)	Abi	NA	FLYB:FBgn0020510	FlyBase Name: Abelson interacting protein
gene (<i>Drosophila melanogaster</i>)	Dlg	NA	FLYB:FBgn0001624	FlyBase Name: discs large 1
gene (<i>Drosophila melanogaster</i>)	Fat2	NA	FLYB:FBgn0261574	FlyBase Name: kugelei
gene (<i>Drosophila melanogaster</i>)	Lar	NA	FLYB:FBgn0000464	FlyBase Name: Leukocyte-antigen-related-like
gene (<i>Drosophila melanogaster</i>)	Sema5c	NA	FLYB:FBgn0284221	FlyBase Name: Semaphorin 5c
gene (<i>Drosophila melanogaster</i>)	Sra1 (CYFIP)	NA	FLYB:FBgn0038320	FlyBase Name: Cytoplasmic FMR1 interacting protein
genetic reagent (<i>Drosophila melanogaster</i>)	ubi>Abi-mCherry	Bloomington <i>Drosophila</i> Stock Center; FLYB:FBfr0227194 (S. Huelsmann)	FLYB:FBst0058729; BDSC:58729	FlyBase Symbol: P{Ubi-mCherry.Abi}3
genetic reagent (<i>Drosophila melanogaster</i>)	UAS>abi-RNAi	National Institute of Genetics, Japan	NIG:9749R-3	
genetic reagent (<i>Drosophila melanogaster</i>)	Fat2-3xGFP FRT80B	Lab of S. Horne-Badovinac; PMID:28292425	FLYB:FBal0326664	FlyBase Symbol: kug[3xGFP]
genetic reagent (<i>Drosophila melanogaster</i>)	fat2 ^{N103-2} FRT80B	Lab of S. Horne-Badovinac; PMID:22413091	FLYB:FBal0267777	FlyBase Symbol: kug[N103-2]
genetic reagent (<i>Drosophila melanogaster</i>)	UAS>fat2-RNAi	Bloomington <i>Drosophila</i> Stock Center; PMID:26320097	FLYB:FBst0040888; BDSC:40888	FlyBase Genotype: y[1] v[1]; P{TRiP.HMS02136}attP40
genetic reagent (<i>Drosophila melanogaster</i>)	hs>Flp	Lab of Richard Fehon	FLYB:FBti0000784	FlyBase Symbol:P{hsFLP}12
genetic reagent (<i>Drosophila melanogaster</i>)	FRT40A	Bloomington <i>Drosophila</i> Stock Center; PMID:8404527	FLYB:FBti0002071	FlyBase Symbol: P{neoFRT}40A
genetic reagent (<i>Drosophila melanogaster</i>)	FRT80B	Bloomington <i>Drosophila</i> Stock Center; PMID:8404527	FLYB:FBti0002073	FlyBase Symbol: P{neoFRT}80B
genetic reagent (<i>Drosophila melanogaster</i>)	act5c>CD2>Gal4, UAS>mRFP-NLS (III)	Bloomington <i>Drosophila</i> Stock Center; PMID:9053304	FLYB:FBst0030558; BDSC:30558	
genetic reagent (<i>Drosophila melanogaster</i>)	t155>Gal4 UAS>Flp	Lab of David Bilder; original source PMID:9584125	FLYB:FBst0005080; BDSC:5080	FlyBase Genotype: y[1] w*; P{GawB}T155 P{UAS-FLP.D}JD2
genetic reagent (<i>Drosophila melanogaster</i>)	tj>Gal4		FLYB:FBtp0089190; DGRC:104055	FlyBase Symbol: P{tj-GAL4.U}
genetic reagent (<i>Drosophila melanogaster</i>)	UAS>GrabFP-A ^{HL} -mCherry	Bloomington <i>Drosophila</i> Stock Center; PMID:28395731	FLYB:FBst0068178; BDSC:68178	
genetic reagent (<i>Drosophila melanogaster</i>)	lar ^{13.2} FRT40A	Bloomington <i>Drosophila</i> Stock Center; PMID:8598047	FLYB:FBst0008774; BDSC:8774	
genetic reagent (<i>Drosophila melanogaster</i>)	lar ^{bola1}	Bloomington <i>Drosophila</i> Stock Center; PMID:11688569	FLYB:FBst0091654; BDSC:91654	
genetic reagent (<i>Drosophila melanogaster</i>)	Lar-3xGFP FRT40A	This study		Endog. Lar with C-term. 3xeGFP fusion made by HR using CRISPR/Cas9
genetic reagent (<i>Drosophila melanogaster</i>)	UAS>lar-RNAi	Bloomington <i>Drosophila</i> Stock Center; PMID:26320097	FLYB:FBst0040938; BDSC:40938	
genetic reagent (<i>Drosophila melanogaster</i>)	MKRS hsFLP/TM6b, Cre	Bloomington <i>Drosophila</i> Stock Center	FLYB:FBst0001501; BDSC:1501	y[1] w[67c23]; MKRS, P{hsFLP}86E/TM6B, P{Crew}DH2, Tb[1]
genetic reagent (<i>Drosophila melanogaster</i>)	nanos-Cas9	Bloomington <i>Drosophila</i> Stock Center; FLYB:FBfr0223952 (F. Port & S. Bullock); PMID:25002478	FLYB:FBst0054591; BSDC:54591	FlyBase Genotype: y[1] M{nos-Cas9.P}ZH-2A w*
genetic reagent (<i>Drosophila melanogaster</i>)	ubi>mRFP-NLS (2L) FRT40A	Bloomington <i>Drosophila</i> Stock Center	FLYB:FBst0034500; BDSC:34500	
genetic reagent (<i>Drosophila melanogaster</i>)	ubi>mRFP-NLS (3L) FRT80B	Bloomington <i>Drosophila</i> Stock Center; FLYB:FBfr0210705 (J. Lipsick)		FlyBase Genotype: w1118; P{Ubi-mRFP.nls}3L P{neoFRT}80B
genetic reagent (<i>Drosophila melanogaster</i>)	Sema5c ^{K175} FRT80B	Lab of S. Horne-Badovinac; PMID:30827914	FLYB:FBal0347471	
genetic reagent (<i>Drosophila melanogaster</i>)	Sema5c-3xGFP FRT80B	Lab of S. Horne-Badovinac; PMID:30827914	FLYB:FBal0347472	
genetic reagent (<i>Drosophila melanogaster</i>)	Sra1-GFP FRT80B	Lab of S. Horne-Badovinac; PMID:36154691	FLYB:FBal0385621	
genetic reagent (<i>Drosophila melanogaster</i>)	w ¹¹¹⁸	Bloomington <i>Drosophila</i> Stock Center	FLYB:FBal0018186	
antibody	Discs Large; Dlg (mouse monoclonal)	Developmental Studies Hybridoma Bank	DSHB:4F3; RRID:AB_528203	Used at 1:20, overnight at 4°C
antibody	Lar (mouse monoclonal)	Developmental Studies Hybridoma Bank	DSHB:9D82B3	Used at 1:200, overnight at 4°C
antibody	Alexa Fluor™ 647, donkey anti-mouse secondary	Thermo Fisher Scientific	Cat:A31571; RRID:AB_162542	Used at 1:300, 3 hrs at room temp
chemical compound, drug	CellMask™ Orange Plasma Membrane Stain	Thermo Fisher Scientific	Cat:C10045	Used at 1:250, 15 min
chemical compound, drug	EGTA 0.5M aq. soln.	Thermo Fisher Scientific	Cat:J60767	Used at 20 mM
chemical compound, drug	TRITC Phalloidin	Millipore Sigma	Cat:1951	Used at 1:300, 15 min at room temp
chemical compound, drug	Alexa Fluor™ 647 phalloidin	Thermo Fisher Scientific	Cat:A22287	Used at 1:50, 3 hrs at room temp
chemical compound, drug	CK-666, Arp2/3 complex inhibitor	Millipore Sigma	Cat:553502	Used at 750 μM
chemical compound, drug	Formaldehyde, 16%, methanol free, ultra pure	Polysciences	Cat:18814-10	
chemical compound, drug	Recombinant human insulin	Millipore Sigma	Cat:12643	
recombinant DNA reagent	plasmid: pU6-BbsI-chiRNA	Addgene	Addgene:45946; RRID:Addgene_45946	PMID:23709638
recombinant DNA reagent	plasmid: pU6 chiRNA Lar C-term	This study		CRISPR chiRNA construct for generation of Lar-3xGFP

recombinant DNA reagent	plasmid: pDsRed-attP	Addgene	Addgene:51019	Vector used to make pDsRed-attP Lar-3xGFP HR
recombinant DNA reagent	plasmid: pDsRed-attP Lar3xGFP HR	This study		CRISPR homologous recombination construct for generation of Lar-3xGFP
software, algorithm	Zen Blue	Zeiss		
software, algorithm	FIJI (ImageJ)	PMID:22743772; 26153368		
software, algorithm	GraphPad Prism 9 for Mac	GraphPad Software		
software, algorithm	Microsoft Excel for Mac, version 16.47	Microsoft		
software, algorithm	Python 3	Python Software Foundation		https://www.python.org
software, algorithm	cellpose	Carson Stringer and Marius Pachitariu, PMID:		https://cellpose.org ; DOI:10.1038/s41592-020-01018-x
software, algorithm	imageio	imageio contributors		https://imageio.readthedocs.io
software, algorithm	matplotlib	The Matplotlib Development team		https://matplotlib.org
software, algorithm	napari	napari contributors		https://napari.org ; DOI:10.5281/zenodo.7276432
software, algorithm	numpy	numpy contributors		https://numpy.org/
software, algorithm	pims	pims contributors		http://soft-matter.github.io/pims/v0.5
software, algorithm	pandas	pandas contributors		https://pandas.pydata.org
software, algorithm	scikit-image	scikit-image development team		https://scikit-image.org ; DOI:10.7717/peerj.453
software, algorithm	scikit-ffm	scikit-ffm contributors		https://pythonhosted.org/scikit-ffm
software, algorithm	scipy	scipy contributors		https://scipy.org ; DOI:10.1038/s41592-019-0686-2

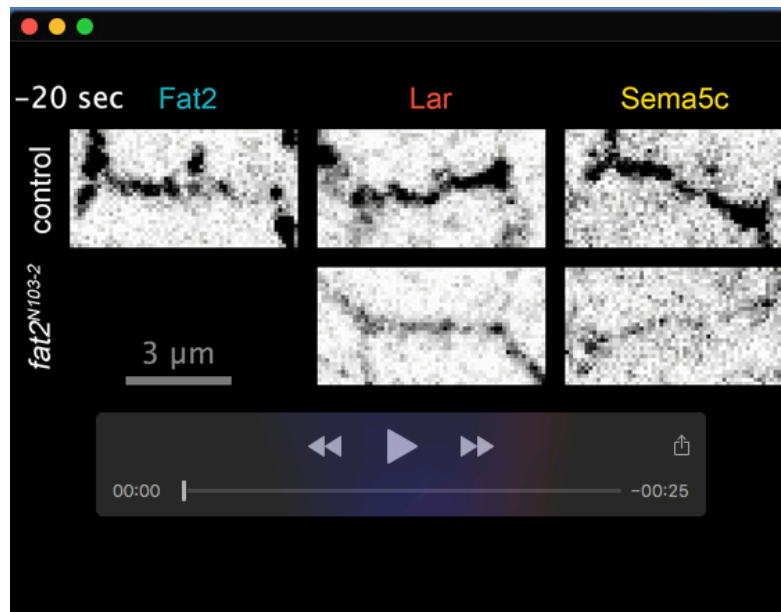
Table S2. Genotypes of experimental animals

Figure	Panel	Brief name or label	Genotype
1	B	Sra1	w ¹¹¹⁸ ;; FRT82B Sra1-GFP/+
	C	Fat2	w ¹¹¹⁸ ; tj>Gal4, UAS>Flp/+; Fat2-3xGFP FRT80B/FRT80B
		Lar	w ¹¹¹⁸ ; Lar-3xGFP FRT40A/FRT40A; t155>Gal4, UAS>Flp/+
		Sema5c	w ¹¹¹⁸ ; tj>Gal4, UAS>Flp/+; Sema5c-3xGFP FRT80B/FRT80B
	E,F	Fat2	w ¹¹¹⁸ ;; ubi>Abi-mCherry, Fat2-3xGFP FRT80B/Fat2-3xGFP FRT80B
		Lar	w ¹¹¹⁸ ; Lar-3xGFP FRT40A ; ubi>Abi-mCherry/+
Sema5c		w ¹¹¹⁸ ;; ubi>Abi-mCherry, Sema5c-3xGFP FRT80B/Sema5c-3xGFP FRT80B	
2	A,B	Sema5c in fat2-RNAi mosaic epithelium	hs>Flp, w ¹¹¹⁸ ; UAS>fat2-RNAi/+ ; Sema5c-3xGFP FRT80/act5c>CD2>Gal4, UAS>mRFP-NLS
	C,D	Sema5c in lar ^{13.2} mosaic epithelium	w ¹¹¹⁸ ; lar ^{13.2} FRT40A/ubi>mRFP-NLS FRT40A ; Sema5c-3xGFP FRT80B/t155>Gal4, UAS>Flp
	E	fat2-RNAi / Control	hs>Flp, w ¹¹¹⁸ ; UAS>fat2-RNAi/+ ; Sema5c-3xGFP FRT80/act5c>CD2>Gal4, UAS>mRFP-NLS
		lar ^{13.2} / Control	w ¹¹¹⁸ ; lar ^{13.2} FRT40A/ubi>mRFP-NLS FRT40A ; Sema5c-3xGFP FRT80B/t155>Gal4, UAS>Flp
3	A	All images	w ¹¹¹⁸
	B,C	Fat2	w ¹¹¹⁸ ;; Fat2-3xGFP FRT80B
		Lar	w ¹¹¹⁸ ; Lar-3xGFP FRT40A
		Sema5c	w ¹¹¹⁸ ;; Sema5c-3xGFP FRT80B
D	Fat2	w ¹¹¹⁸ ;; Fat2-3xGFP FRT80B	
4	B-D,F	Control	w ¹¹¹⁸ ; tj>Gal4/+ ; Fat2-3xGFP FRT80/+
		+GrabFP-A ^{int}	w ¹¹¹⁸ ; tj>Gal4/+ ; Fat2-3xGFP FRT80/UAS>GrabFP-A ^{int} -mCherry
5	A,B	Control	w ¹¹¹⁸ ; tj>Gal4/+
		lar-RNAi	w ¹¹¹⁸ ; tj>Gal4/UAS>lar-RNAi
		Sema5c ^{K175}	w ¹¹¹⁸ ; tj>Gal4/+ ; Sema5c ^{K175} FRT80B
		lar-RNAi, Sema5c ^{K175}	w ¹¹¹⁸ ; tj>Gal4/UAS>lar-RNAi ; Sema5c ^{K175} FRT80B
	C	Control	w ¹¹¹⁸ ; tj>Gal4/+
	lar-RNAi	w ¹¹¹⁸ ; tj>Gal4/UAS>lar-RNAi	
6	B-E	Fat2	w ¹¹¹⁸ ;; Fat2-3xGFP FRT80B
		Lar	w ¹¹¹⁸ ; Lar-3xGFP FRT40A
		Sema5c	w ¹¹¹⁸ ;; Sema5c-3xGFP FRT80B
7	A-E	Control (w ¹¹¹⁸)	w ¹¹¹⁸
		fat2 ^{N103-2}	w ¹¹¹⁸ ;; fat2 ^{N103-2} FRT80B
		lar ^{13.2/bola1}	w ¹¹¹⁸ ; lar ^{13.2} FRT40A/lar ^{bola1}
		Sema5c ^{K175}	w ¹¹¹⁸ ;; Sema5c ^{K175} FRT80B
		tj-Gal4, lar-RNAi, Sema5c ^{K175}	w ¹¹¹⁸ ; tj>Gal4/UAS>lar-RNAi ; Sema5c ^{K175} FRT80B
	B	Control (tj-Gal4)	w ¹¹¹⁸ ; tj>Gal4/+
		tj-Gal4, lar-RNAi	w ¹¹¹⁸ ; tj>Gal4/UAS>lar-RNAi
	tj-Gal4, Sema5c ^{K175}	w ¹¹¹⁸ ; tj>Gal4/+ ; Sema5c ^{K175} FRT80B	
C,D	CK-666	w ¹¹¹⁸	
S1	A	Lar-3xGFP	w ¹¹¹⁸ ; Lar-3xGFP FRT40A
		anti-Lar	w ¹¹¹⁸
	B,C	Control	w ¹¹¹⁸
		Lar-3xGFP x1	w ¹¹¹⁸ ; Lar-3xGFP FRT40A/+
		Lar-3xGFP x2	w ¹¹¹⁸ ; Lar-3xGFP FRT40A
	B	lar ^{13.2/bola1}	w ¹¹¹⁸ ; lar ^{13.2} FRT40A/lar ^{bola1}
D-F	Lar in fat2 ^{N103-2} mosaic epithelium	w ¹¹¹⁸ ; Lar-3xGFP FRT40A/tj>Gal4, UAS>Flp ; fat2 ^{N103-2} FRT80B/ubi>mRFP-NLS FRT80B	
S2	A	All	hs>Flp, w ¹¹¹⁸ ; UAS>fat2-RNAi/+ ; Sema5c-3xGFP FRT80/act5c>CD2>Gal4, UAS>mRFP-NLS
	B	Control	w ¹¹¹⁸ ;; Sema5c-3xGFP FRT80B
		fat2 ^{N103-2}	w ¹¹¹⁸ ;; Sema5c-3xGFP fat2 ^{N103-2} FRT80B
	C	Control	w ¹¹¹⁸ ;; Sema5c-3xGFP FRT80B/UAS>Abi-RNAi
	abi-RNAi	w ¹¹¹⁸ ; tj>Gal4/+ ; Sema5c-3xGFP FRT80B/UAS>Abi-RNAi	
S3	A-C	Lar	w ¹¹¹⁸ ; Lar-3xGFP FRT40A
		Lar fat2 ⁻	w ¹¹¹⁸ ; Lar-3xGFP FRT40A ; fat2 ^{N103-2} FRT80B
	D-F	Sema5c	w ¹¹¹⁸ ;; Sema5c-3xGFP FRT80B
		Sema5c fat2 ⁻	w ¹¹¹⁸ ;; Sema5c-3xGFP fat2 ^{N103-2} FRT80B
	G	Fat2	w ¹¹¹⁸ ;; Fat2-3xGFP FRT80B
		Lar	w ¹¹¹⁸ ; Lar-3xGFP FRT40A
		Sema5c	w ¹¹¹⁸ ;; Sema5c-3xGFP FRT80B
	H	Fat2-3xGFP x1	w ¹¹¹⁸ ;; Fat2-3xGFP FRT80B/+
Fat2-3xGFP x2		w ¹¹¹⁸ ;; Fat2-3xGFP FRT80B	

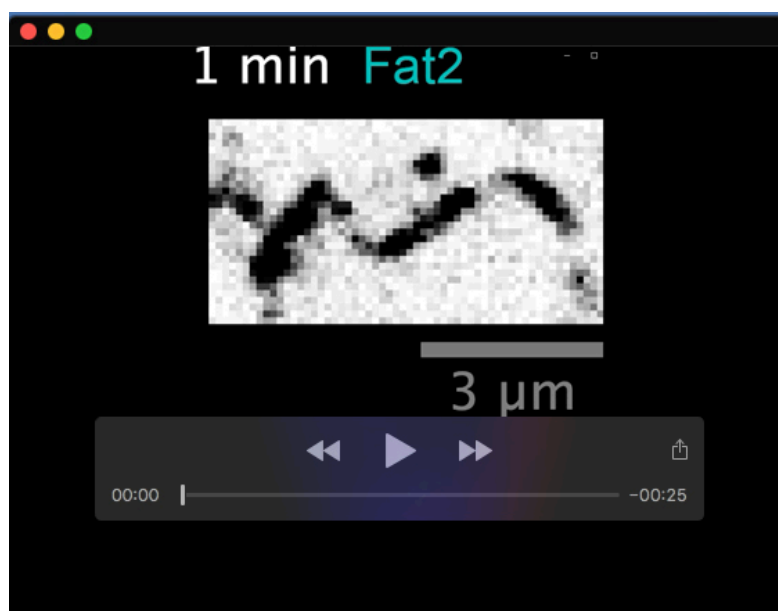
		Lar-3xGFP x1	w ¹¹¹⁸ ; Lar-3xGFP FRT40A/+
		Lar-3xGFP x2	w ¹¹¹⁸ ; Lar-3xGFP FRT40A
		Sema5c-3xGFP x1	w ¹¹¹⁸ ;; Sema5c-3xGFP FRT80B/+
		Sema5c-3xGFP x2	w ¹¹¹⁸ ;; Sema5c-3xGFP FRT80B
S4	A,B	Control (w ¹¹¹⁸)	w ¹¹¹⁸
		fat2 ^{N103-2}	w ¹¹¹⁸ ;; fat2 ^{N103-2} FRT80B
		lar ^{13.2/bola1}	w ¹¹¹⁸ ; lar ^{13.2} FRT40A/lar ^{bola1}
		Sema5c ^{K175}	w ¹¹¹⁸ ;; Sema5c ^{K175} FRT80B
		tj-Gal4, lar-RNAi, Sema5c ^{K175}	w ¹¹¹⁸ ; tj>Gal4/UAS>lar-RNAi; Sema5c ^{K175} FRT80B

Table S3. *Drosophila* culture conditions for experiments

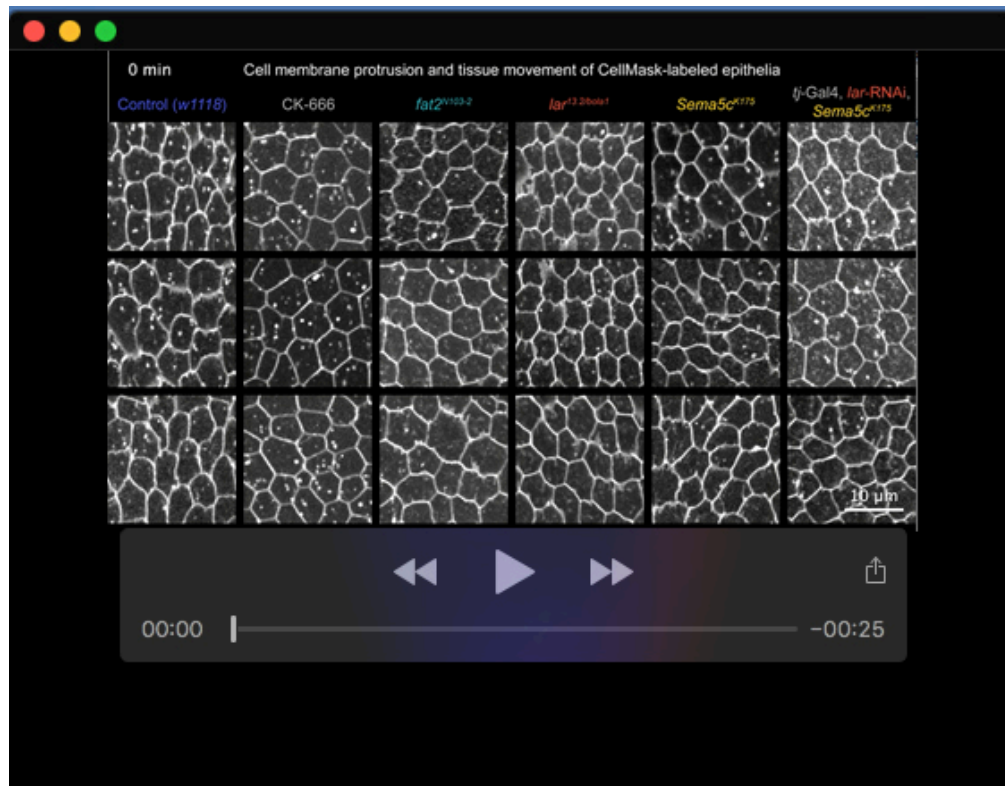
Figure	Panel	Days on yeast	Temp (°C)
1	B	2-3	25
	C - Fat2	3	25
	C - Lar	5	25
	C - Sema5c	3	25
	E,F	2-3	25
2	A,B	See methods for heat shock protocol	
	C,D	5	25
	E	see A,B and C,D	
3	A-D	2-3	25
4	B-D,F	3	29
5	A-C	3	29
6	B-E	2	25
7	A,C-E, B gray background (except tj-Gal4, lar-RNAi, Sema5c ^{K175} condition)	2	25
	tj-Gal4, lar-RNAi, Sema5c ^{K175} condition in A,C-E, B gray background	2	29
	B white background	2	29
S1	A	2-3	25
	B,C	2	25
	D-F	3	25
S2	A	See methods for heat shock protocol	
	B	2	25
	C	3	29
S3	A-F	2	25
	G,H	2-3	25
S4	All but tj-Gal4, lar-RNAi, Sema5c ^{K175}	2	25
	tj-Gal4, lar-RNAi, Sema5c ^{K175}	2	29



Movie 1. FRAP of Fat2-3xGFP, Lar-3xGFP, and Sema5c-3xGFP at interfaces in control and *fat2*^{N103-2} epithelia. Movies begin 20 seconds before photobleaching and follow leading-trailing interfaces (control) or similarly-oriented inter-faces (*fat2*^{N103-2}) for the subsequent 8 minutes. Display brightness settings are adjusted separately for each fluorophore, but preserved between control and *fat2*^{N103-2} conditions. Associated with Figs. 6B,D; S3A-F.



Movie 2. FRAP of Fat2-3xGFP at a leading-trailing interface over 30 minutes. The timelapse movie follows fluorescence recovery at a leading-trailing interface beginning one minute before photobleaching. Associated with Fig. 6C,E.



Movie 3. Effects of loss of Fat2, Lar, and Sema5c on migration and membrane protrusion dynamics. Timelapse movies of the basal surfaces of epithelia labeled with CellMask membrane dye. Several examples from each condition are shown. Associated with Figs. 7; S4.